Full title: Activity-dependent synapse clustering underlies eye-specific competition in the developing retinogeniculate system

Short title: Activity-dependent synaptic clustering underlies eye-specific competition

Author list: Chenghang Zhang[1], Tarlan Vatan[1], and Colenso M. Speer[1,*]

Author Affiliations: [1] Department of Biology, University of Maryland, College Park, Maryland, USA. 20742.

[*]Corresponding author

E-mail: cspeer@umd.edu (CS)

Abstract

Co-active synaptic connections are often spatially clustered to facilitate local dendritic computations underlying learning, memory, and basic sensory processing. In the mammalian visual system, retinal ganglion cell (RGC) axons converge to form clustered synaptic inputs that enable local signal integration in the dorsal lateral geniculate nucleus (dLGN) of the thalamus. While visual experience promotes retinogeniculate synapse clustering after eye-opening, the earliest events in cluster formation prior to visual experience are unknown. Here, using volumetric super-resolution single-molecule localization microscopy and eye-specific labeling of developing retinogeniculate synapses in mice, we show that synaptic clustering is eye-specific and activity-dependent during retinogeniculate refinement in the first postnatal week. We identified a subset of retinogeniculate synapses with multiple active zones that are surrounded by like-eye synapses and depleted of synapse clustering from the opposite eye. In mutant mice with disrupted spontaneous retinal wave activity, synapses with multiple active zones still form, but do not exhibit the synaptic clustering seen in controls. These results highlight a role for spontaneous retinal activity in regulating eye-specific synaptic clustering in circuits essential for visual perception and behavior.

Introduction

A key mechanism for neuronal signal processing is the formation of spatially clustered synaptic inputs, which facilitate local computations within individual dendrites (1-3). Through biophysical signal integration mechanisms, these synaptic clusters play critical

34 computational roles in learning, memory, and sensory processing underlying cognition
35 and behavior (4-7). During circuit development, the formation of synaptic clusters is
36 regulated by both spontaneous and sensory-driven neural activity, which helps to
37 stabilize or eliminate individual synapses and establish mature connectivity patterns (5,
38 6, 8).
39
40 A model example of activity-dependent synaptic cluster formation is the refinement of
41 retinal inputs to the dorsal lateral geniculate nucleus (dLGN) of the thalamus (9).
42 Electron microscopy (EM) reconstructions of the mouse dLGN show that retinal
43 ganglion cell (RGC) inputs converge to form “complex” synaptic clusters known as
44 glomeruli (10-14). Each glomerulus contains multiple RGC axon terminal boutons
45 formed onto a dendritic branch of a dLGN relay neuron. These boutons vary from small
46 terminals with a single active zone (AZ) to large or perforated synapses containing
47 multiple AZs (10-13). Ultrastructural evidence of synaptic integration is supported by
48 experiments using transsynaptic (15) and Brainbow-based RGC labeling (11, 13),
49 optogenetic stimulation of RGC axons (16, 17), and calcium imaging of retinogeniculate
50 boutons (18) confirming the clustering of RGC inputs to relay neuron dendrites in the
51 dLGN. Because individual glomeruli often receive inputs from multiple RGCs that
52 encode either similar or distinct visual features (18), proper developmental wiring of
53 RGC bouton clusters is critical for local dendritic integration that drives visual responses
54 in the adult brain.
55

Previous studies have shown that synaptic cluster development in neural circuits depends on spatiotemporally correlated synaptic activity to regulate synaptogenesis, pruning, and plasticity (6, 19). In the developing retinogeniculate system, there are two sources of correlated activity that may contribute to synaptic clustering: 1) visual experience that drives topographic activation of neighboring RGCs and 2) spontaneous retinal wave activity that correlates burst firing of neighboring RGCs prior to eye-opening. Consistent with experience-dependent plasticity, retinogeniculate bouton clustering increases after eye-opening (10, 13, 20) and visual deprivation reduces clustering (20). However, these experience-dependent synaptic clustering effects occur after eye-opening, when eye-specific retinogeniculate segregation is complete (21-23). Before photoreceptor-mediated visual onset, retinal waves generate spatiotemporal correlations in RGC burst activity that are expected to facilitate Hebbian strengthening of co-active synapses (24). Whether this correlated activity promotes retinogeniculate synapse clustering prior to eye-opening is unknown.

To address this question, we used volumetric super-resolution microscopy, anterograde tract tracing, and immunohistochemical synaptic protein labeling to investigate the local spatial relationships between eye-specific synapses in the dLGN prior to photoreceptor-mediated visual experience. During eye-specific segregation (postnatal days 2-8), we identified a subset of retinogeniculate inputs that formed multiple active zones (mAZ synapses), while all other retinal input synapses contained only a single active zone (sAZ synapses). Comparing the spatial relationships between all retinogeniculate synapses, we observed non-random, eye-specific clustering of sAZ synapses around

mAZ synapses. During eye-specific synaptic competition, both the “winning” and “losing” eye-specific inputs showed increased sAZ clustering when like-eye mAZ synapses were in close proximity. In contrast, mAZ synapses from the “losing” eye projection were less clustered when located near a mAZ synapse from the “winning” eye.

These patterns of eye-specific synaptic clustering were absent in a genetic mutant mouse line with abnormal stage II cholinergic retinal waves and retinogeniculate segregation defects. These results demonstrate that spontaneous retinal activity regulates retinogeniculate synaptic clustering prior to eye-opening and are consistent with the action of non-cell-autonomous synaptic stabilization and punishment signals underlying eye-specific competition in the developing visual system.

Results

Retinogeniculate synapses form multiple active zones during eye-specific competition

To investigate synaptic clustering during eye-specific segregation, we reanalyzed a previously published volumetric super-resolution imaging dataset from our laboratory (25). Using volumetric STochastic Optical Reconstruction Microscopy (STORM) (26), we collected super-resolution imaging data from the dLGNs of wild-type (WT) mice at three postnatal time points (P2, P4, and P8) (Figure 1A). We labeled eye-specific synapses by monocular injection of Alexa Fluor-conjugated cholera toxin subunit B tracer (CTB) together with immunostaining for presynaptic Bassoon, postsynaptic

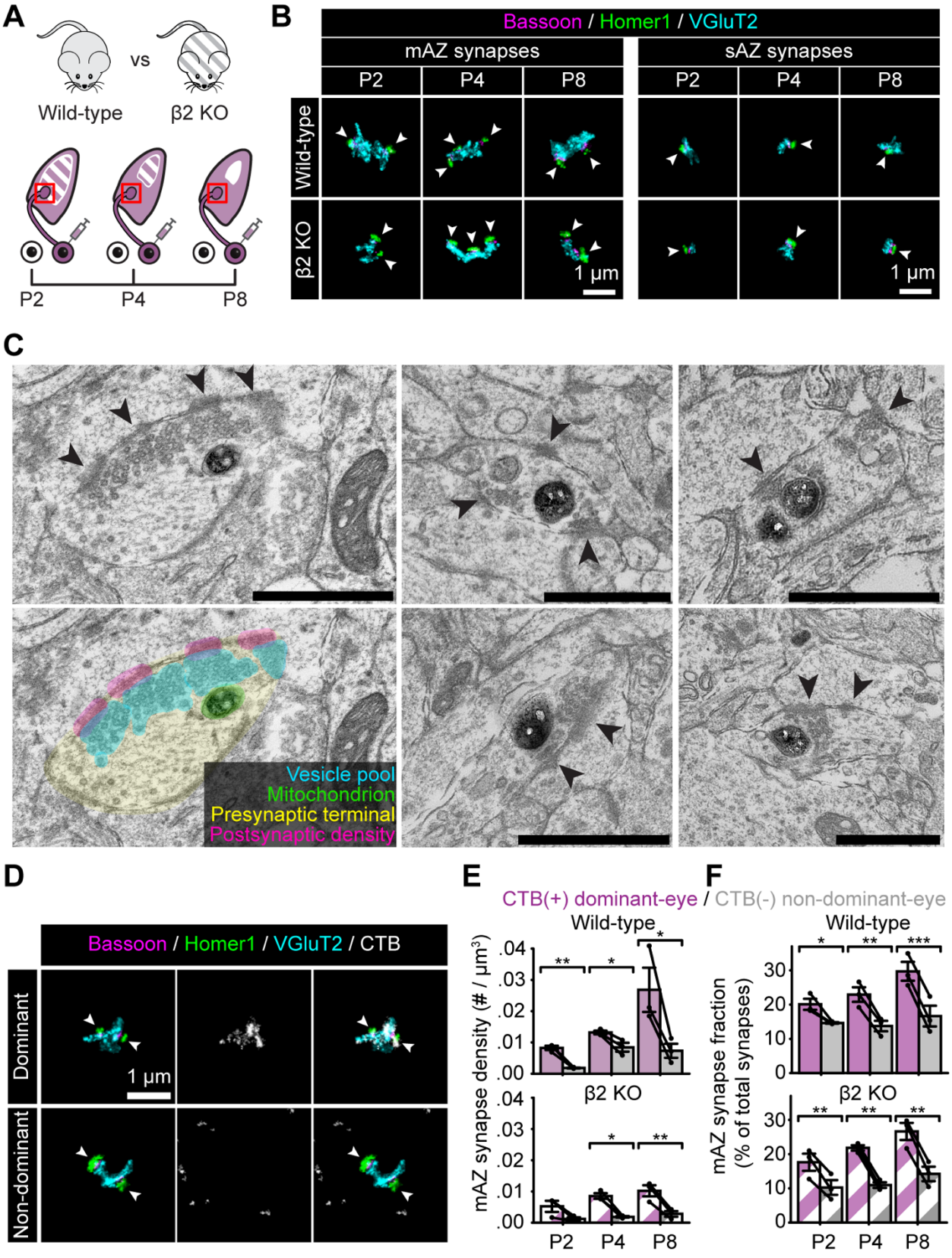

102

103

Figure 1: Retinogeniculate synapses form multiple active zones during eye-specific competition. (A) Experimental design: CTB-Alexa 488 was injected into the right eye of wild-type (WT) and β2KO mice. One day after the treatment, tissue was collected from the left dLGN at P2, P4, and P8. The red squares indicate the STORM imaging regions. (B) Representative multi-active zone (mAZ, left panels) and single-active zone (sAZ, right panels) synapses in WT (top panels) and β2KO mice (bottom panels) at each age. Arrowheads point to individual Bassoon clusters (active zones) within each synapse. (C) Representative images of mAZ retinogeniculate synapses in the mouse dLGN at P8. Electron microscopy images show darkly-stained dAPEX2(+) mitochondria within RGC boutons. Arrowheads point to electron-dense material at the postsynaptic density (PSD) apposed to individual active zones with clustered presynaptic synaptic vesicles. Scale bars are 1 μm in all images. (D) Representative CTB(+) dominant-eye (top panels) and CTB(-) non-dominant-eye (bottom panels) mAZ synapses in a WT P8 sample, showing synaptic (left panels), CTB (middle panels), and merged immunolabels (right panels). (E and F) Eye-specific mAZ synapse density (E) and mAZ synapse fraction (F) across development in WT (top panel) and β2KO mice (bottom panel). Black dots represent mean values from separate biological replicates and black lines connect measurements within each replicate (N=3 for each age and genotype). Error bars represent group means ± SEMs. Statistical significance between CTB(+) and CTB(-) synapse measurements was assessed using paired T-tests. *: $p<0.05$, **: $p<0.01$, ***: $p<0.001$.

104

105

106

107

Homer1, and presynaptic vesicular glutamate transporter 2 (VGluT2) proteins (25). We collected separate image volumes (~45K μm^3 each) from three biological replicates at each developmental time point. To assess the impact of spontaneous retinal activity on synaptic development across the same time period, we performed identical experiments in a knockout mouse line lacking the beta 2 subunit of the nicotinic acetylcholine receptor (β2KO), which disrupts spontaneous cholinergic retinal wave activity, eye-specific axonal segregation, and retinogeniculate synapse development (21, 25, 27-35). Because eye-specific segregation is incomplete until ~P8, we limited our analysis to the future contralateral eye-specific region of the dLGN, which is reliably identified across all stages of postnatal development (Figure 1A, see also Materials and Methods).

Across our dataset containing tens of thousands of identified synapses (Supplemental Table 1) collected from different ages and genotypes, STORM images revealed two subtypes of retinogeniculate synapses distinguished by the number of active zones (AZs) in the presynaptic terminal (Figure 1B). One subtype included synapses with multiple (2-4) Bassoon(+) AZs (hereafter referred to mAZ synapses), while the other consisted of retinogeniculate synapses with a single Bassoon(+) AZ (sAZ synapses) (Figures 1B and S1A). Each mAZ synapse could be a single terminal, or, alternatively, several clustered RGC boutons each of which is a sAZ synapse (10-13). To examine the ultrastructure of mAZ synapses, we used electron microscopy (EM) to image retinogeniculate boutons in the dLGN. We generated a transgenic mouse line expressing the mitochondrial matrix-targeted dimeric dAPEX2 reporter (36) in ipsilaterally projecting RGCs (37) to provide unambiguous mitochondrial labeling in

RGC axons and synaptic terminals. EM images confirmed the presence of large retinogeniculate terminals with multiple active zones, consistent with our STORM data (Figure 1C).

Because our previous analysis of retinogeniculate synaptic refinement reported global changes in eye-specific synapse density regardless of AZ number (25), we first sought to separate mAZ and sAZ synapses and determine their relative densities and ratios during eye-specific segregation. To determine the eye-of-origin for each retinogeniculate synapse, we measured the colocalization of CTB signal with VGluT2 (Figure 1D). By imaging in the contralateral eye-specific region relative to the CTB-injected eye, we defined CTB(+) VGluT2 clusters as “dominant-eye” synapses. Conversely, CTB(-) VGluT2 clusters were classified as “non-dominant eye” synapses. Our previous analysis of binocular CTB control injection data confirmed the high efficiency of retinogeniculate synapse labeling by anterograde tracing (>97% of synapses labeled at P4 and P8), thereby enabling accurate assignment of eye-specific synapses in the mouse brain (25).

After assigning eye-of-origin to all retinogeniculate synapses, we observed that the density of CTB(+) mAZ synapses was significantly higher than CTB(-) mAZ synapses at every age (Figure 1E). In contrast, sAZ density showed eye-specific differences at P2 and P8, but not at P4 (Figure S1B, 5/95% difference confidence interval -0.021~0.008 synapses / μm^3). By adding eye-specific mAZ and sAZ numbers, we found that at P4 the total synapse density is equivalent between the two eyes (5/95% difference

confidence interval -0.014~0.011 synapses / μm^3) and this effect is driven by an increase in the number of CTB(-) ipsilateral sAZ synapses at P4 (Figure S1B). This effect was not seen in β2KO mice, which showed eye-specific differences in the density of both mAZ and sAZ synapses at P4 (Figure 1E and S1B, 5/95% difference confidence interval 0.004~0.010 mAZ synapses / μm^3 and 0.007~0.020 sAZ synapses / μm^3 at P4). In WT mice, the fraction of dominant-eye mAZ synapses was ~20% at P2 and ~29% at P8 while non-dominant-eye mAZ synapses comprised~14% and ~17% at the same time points (Figure 1F, upper panel). In β2KO mice, dominant-eye mAZ synapses represented 17/23% (P2/8) and non-dominant eye mAZ synapses accounted for 10/14% (P2/P8) of the total population. These results indicate that a population of mAZ synapses still forms in β2KO mice despite an overall reduction in synapse density when spontaneous retinal activity is disrupted (25).

Multi-active zone synapses undergo eye-specific vesicle pool maturation

In our previous study of retinogeniculate refinement, we reported eye-specific differences in VGluT2 volume underlying synaptic competition, but did not investigate the relative maturation of presynaptic vesicle pools in sAZ and mAZ synapses (25). To determine these differences, we measured the total VGluT2 volume for mAZ and sAZ synapses. In WT mice, both mAZ (Figure 2A, left panel) and sAZ (Figure 2B, left panel) synapses showed eye-specific differences in presynaptic VGluT2 volume at each time point. During eye-specific competition at P4 in WT mice, the median dominant-eye VGluT2 cluster volume was 372% larger (marginal mean with 95% confidence interval

177 on a logarithmic scale: 0.551 ± 0.294 $\log_{10}[\mu m^3]$) compared to non-dominant-eye
178 synapses (Figure 2A, left panel). In contrast, β2KO mice showed a smaller difference
179 (110%, marginal mean with 95% confidence interval on a logarithmic scale: 0.279 ±
180 0.107 $\log_{10}[\mu m^3]$) between eye-specific mAZ synapse VGluT2 volumes at the same time
181 point (Figure 2A, right panel). For sAZ synapses at P4, the magnitudes of eye-specific
182 differences in VGluT2 volume were significantly smaller: 135% in WT, (Figure 2B, left
183 panel, marginal mean with 95% confidence interval of CTB-specific difference on a
184 logarithmic scale: 0.337 ± 0.275 $\log_{10}[\mu m^3]$, the difference of CTB-specific contrast
185 between mAZ and sAZ synapses: 0.214 ± 0.102 $\log_{10}[\mu m^3]$) and 41% inβ2KO) (Figure
186 2B, right panel, marginal mean with 95% confidence interval of CTB-specific difference
187 on a logarithmic scale: 0.167 ± 0.119 $\log_{10}[\mu m^3]$, the difference of CTB-specific contrast
188 between mAZ and sAZ synapses: 0.112 ± 0.040 $\log_{10}[\mu m^3]$). These data show that the
189 eye-specific pool size differences in mAZ synapses are 2.76-fold greater in WT and
190 2.68-fold greater in β2KO compared to sAZ synapses, indicating that synapse type-
191 specific differences persist despite defects in retinal waves.

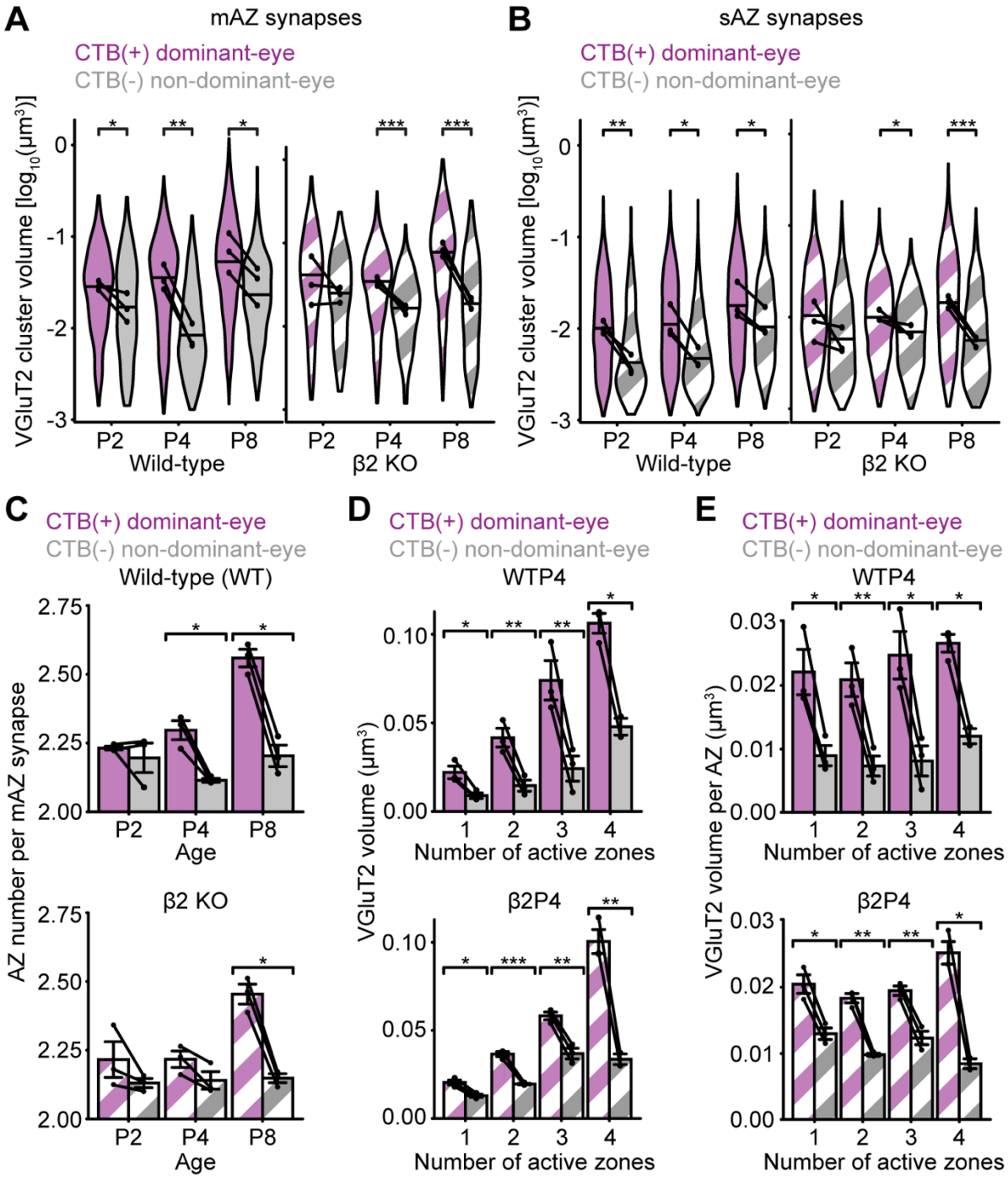

192

Figure 2: Multi-active zone synapses undergo eye-specific vesicle pool maturation. (A) Violin plots showing the distribution of VGluT2 cluster volume for mAZ synapses in WT and β2KO mice at each age. The width of each violin plot reflects the relative synapse proportions at each volume across the entire grouped data set (N=3 biological replicates). The maximum width of the violin plots was normalized across mAZ and sAZ groups. The black dots represent the median value of each biological replicate (N=3), and the black horizontal lines represent the median value of all synapses grouped across replicates. Black lines connect measurements of CTB(+) and CTB(-) populations from the same biological replicate. Statistical significance was determined using a mixed model ANOVA. Black asterisks indicate significant eye-specific differences at each developmental time point. (B) Violin plots similar to (A) show the distributions of VGluT2 cluster volume for sAZ synapses in WT and β2KO mice at each age. (C) Average number of AZs (individual bassoon clusters) per mAZ synapse in WT (top panel) and β2KO mice (bottom panel). Black dots represent mean values from separate biological replicates and black lines connect measurements within each replicate. (D and E) Total (D) and average/AZ (E) VGluT2 cluster volume as a function of AZ number for all synapses in WT P4 samples (top panel) and β2KO P4 samples (bottom panel). Black dots represent mean values from separate biological replicates and black lines connect measurements within each replicate. A table of the total eye-specific synapse numbers of each type (mAZ and sAZ) and AZ number for each biological replicate in both genotypes is included in the Supplemental Materials (Table S1). In (C-E), error bars represent means ± SEMs. Statistical significance was assessed using paired T-tests. In all panels, *: $p<0.05$, **: $p<0.01$, ***: $p<0.001$. N=3 biological replicates for each age and genotype.

193

194

To determine if the presynaptic vesicle pool volume scales with the number of active zones, we compared the number of Bassoon clusters toVGluT2 cluster volume for each mAZ synapse. In both WT (Figure 2C, top panel) and β2KO mice (Figure 2C, bottom panel), mAZ synapses were associated with an average of 2-3 Bassoon clusters in the first postnatal week. In WT mice, the number of AZs in CTB(+) dominant-eye mAZ synapses was significantly higher than in non-dominant CTB(-) mAZ synapses at P4 and P8 (Figure 2C, top panel). However, this difference was not observed at P4 in β2KO mice (Figure 2C, bottom panel. 5/95% confidence interval -0.0005~0.015). For CTB(+) dominant-eye synapses in both WT and β2KO mice, vesicle pool size was positively correlated with AZ number (Figure 2D, Figure S2A/B; correlation coefficients: WT [0.99] and β2KO [0.95]). This correlation was also present for CTB(-) non-dominant-eye synapses, but with a smaller magnitude at P4 and P8 (correlation coefficients: WT [0.97] and β2KO [0.90]. Dividing the total presynaptic VGluT2 volume by the AZ number revealed a consistent vesicle volume per AZ for both sAZ and mAZ synapses(Figure 2E, S2C/D). In dominant-eye CTB(+) synapses, 5/95% confidence intervals of mAZ VGluT2 volume were -61%~50% of sAZ synapses in WT mice and -32%~11% in β2KO mice. In non-dominant-eye CTB(-) synapses, 5/95% confidence intervals of mAZ VGluT2 volume were -88%~51% of sAZ synapses in WT mice and -43%~5% in β2KO mice. The results indicate that for each synapse, vesicle pool volume increases linearly with the number of AZs.

Multi-active zone synapses are loci for synaptic clustering

Eye-specific competition is thought to result from the stabilization of co-active dominant-eye RGC inputs and the elimination of non-dominant-eye inputs that are out of sync with neighboring synapses (38-40). In this context, mAZ synapses with greater release probability may play an important role in the local refinement of nearby synapses (41-43). To determine whether retinogeniculate synapses cluster prior to eye-opening, we measured the proximity of eye-specific sAZ synapses to mAZ synapses and other sAZs synapses. We then compared these distances to a randomized synapse distribution, where sAZ synapse positions were shuffled within the neuropil volume while mAZ positions remained fixed. For every sAZ and mAZ synapse in the dataset, we identified neighboring sAZ synapses as “nearby” when their weighted centroid was within a defined distance from the edge of the target center synapse (Figure 3A, a mAZ synapse in this case). We tested search radii between 1-4 μm around both CTB(+) and CTB(-) mAZ synapses, measuring the ratio of nearby sAZ synapses in the original versus randomized data sets (Figures S3A/B). The largest differences between the original and randomized distributions occurred within 1-2 μm search radius, suggesting non-random clustering of sAZ synapses near mAZ synapses from the same eye (Figure S3A/B). We did not observe this clustering pattern when sAZ synapses and mAZ synapses originated from different eyes (Figure S3C/D). This analysis defined “nearby” sAZ synapses as those within 1.5 μm of a mAZ synapse edge (Figure 3A, S3).

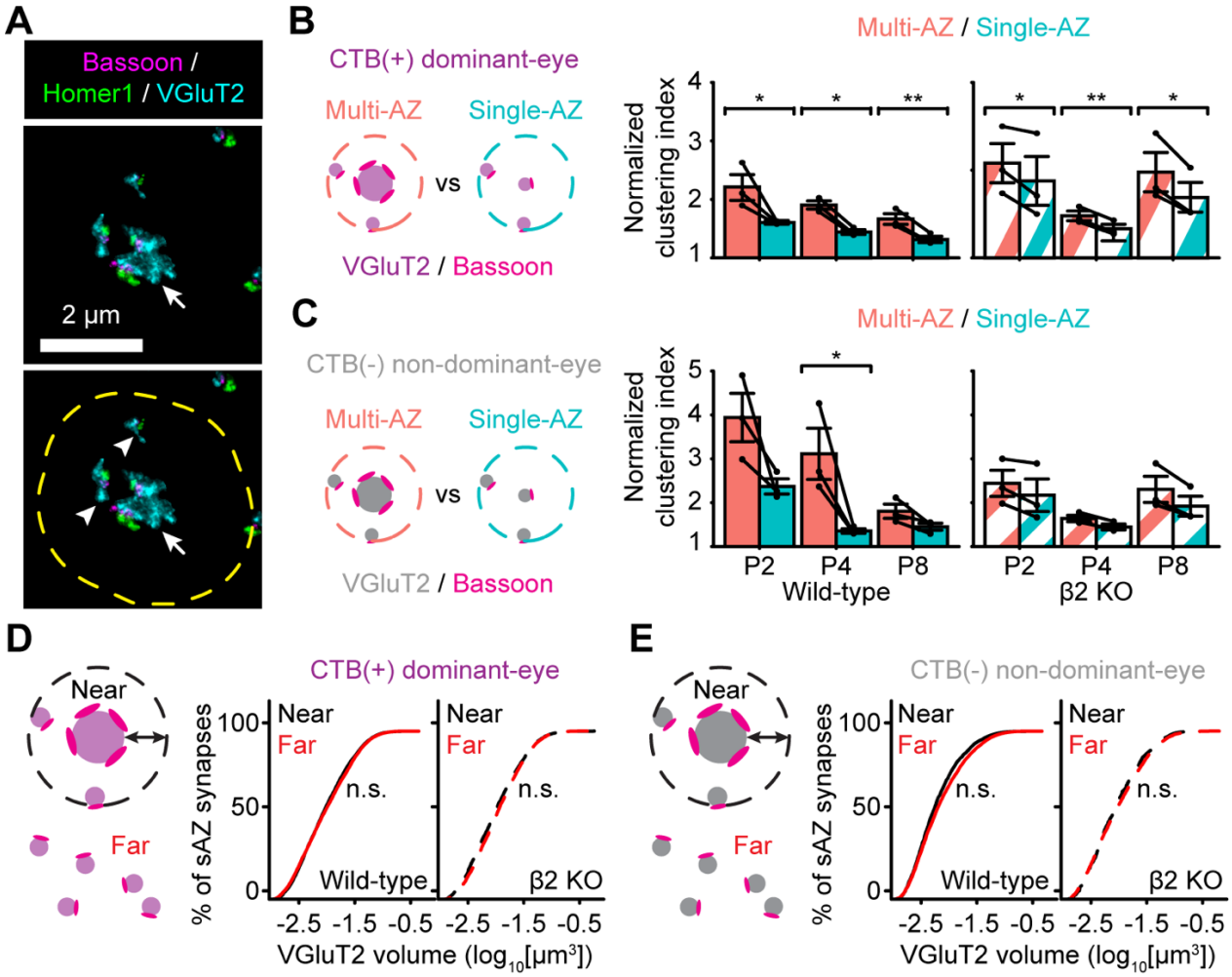

238

Figure 3: Multi-active zone synapses are loci for synaptic clustering. (A) A representative mAZ synapse (arrow) in a WT P8 dLGN with nearby sAZ synapses (arrowheads) clustered within 1.5 μm (dashed yellow ring). (B) Comparison of a normalized clustering index between CTB(+) dominant-eye mAZ and sAZ synapses at each time point in WT (left) and β2KO (right) mice. Black dots represent mean values from separate biological replicates and black lines connect measurements within each replicate (N=3 for each age and genotype). (C) Same as in (B) showing the normalized clustering index measurements for CTB(-) non-dominant-eye synapses. In B/C, paired T-tests were used to test the statistical significance between mAZ and sAZ clustering index measurements. Error bars represent means ± SEMs. *: $p<0.05$; **: $p<0.01$. (D) Cumulative distributions of VGluT2 volume for CTB(+) dominant-eye sAZ synapses near (<1.5 μm, black lines) or far from (>1.5 μm, red lines) like-eye mAZ synapses. Left panel: WT. Right panel: β2KO. (E) Same as in (D) showing the cumulative distributions of VGluT2 volume for CTB(-) non-dominant-eye sAZ synapses relative to like-eye mAZ synapses. The distributions in D/E show merged data across all developmental ages (P2/P4/P8; N=3 biological replicates at each time point). A nonparametric Kolmogorov-Smirnov test was used for statistical analysis. “n.s.” indicates no significant difference between near and far sAZ synapse distributions from the K-S test. Separate measurements of 5/95% confidence intervals show overlap of the two distributions in each case.

In addition to sAZ clustering near mAZ synapses, sAZ synapses also showed a non-random relationship to other sAZ synapses across ages and genotypes (Figure S4A and S4B). Although axonal path lengths were not available in our dataset, our volume-based randomization allowed for direct comparison of clustering magnitudes between mAZ and sAZ synapses. We calculated a clustering index by dividing the “nearby” sAZ synapse ratio (% of total synapses) in the original data by that in the randomized data(Figure 3, B and C). This index revealed that for dominant-eye synapses, greater clustering occurred for mAZ synapses across all ages and genotypes (Figure 3B).

However, for non-dominant eye synapses, the mAZ versus sAZ contrast was only found in WT mice at P4 (Figure 3C). At this stage, ipsilateral RGC axon synaptogenesis continues and ipsilateral sAZ synapses form near mAZ synapses despite being in the future contralateral eye-specific territory. However, after eye-specific competition at P8, non-dominant-eye CTB(-) sAZ synapses were eliminated nearby CTB(-) mAZ synapses from P4-P8, while the mAZ synapses were retained (the 5/95% confidence interval for the change in mAZ synapse density from P4 to P8 in β2KO mice was -0.0011~0.0028 synapses / μm^3) (Figure 1E).

In β2KO mice, dominant-eye projections also showed increased clustering around mAZ synapses compared to sAZ synapses (Figure 3B, right panel), suggesting partial maintenance of synaptic clustering despite retinal wave defects. However, non-dominant eye mAZ synapses in β2KO mice did not show clustering at P4 (Figure 3C, right panel, 5/95% confidence interval: -0.033~0.42), consistent with the overall

reduction in sAZ synapse number compared with WT mice (Figure S1B). Together, these results show that defects in spontaneous retinal activity reduce synaptic clustering in an eye-specific manner.

To validate the robustness of our comparison between original and randomized data across randomization seeds, we quantified the ratio of sAZ synapses nearby mAZ or sAZ center synapses in 10 randomized trials (Figure S4C, representative data from a WTP4 sample). The result showed that variation across 10 randomizations was minimal and did not impact the comparison.

Considering that sAZ synapses show eye-specific differences in vesicle pool volume (Figure 2 A/B) and cluster nearby mAZ synapses (Figure 3 A-C), we hypothesized that mAZ synapses might influence the vesicle pool size of nearby sAZ synapses. To test this, we classified sAZ as “near” (within 1.5 µm of a like-eye mAZ synapse) or “far” (any distance >1.5 µm). Across all ages and genotypes, we found no significant differences in vesicle pool volume between near and far sAZ synapses for either dominant-eye (difference in VGluT2 volume: -0.08 ~ 0.004 $\log_{10}[\mu m^3]$, 5/95% confidence interval) or non-dominant-eye synapses (difference in VGluT2 volume: -0.06 ~ 0.105 $\log_{10}[\mu m^3]$, 5/95% confidence interval) (Figure 3 D/E, displays data merged for all time points). This result shows that sAZ vesicle pool size is independent of their proximity to mAZ synapses.

Synaptic clustering varies with distance to neighboring eye-specific multi-active zone synapses

RGC axon refinement is a dynamic process involving branch stabilization and elimination based on the relative activity patterns among neighboring inputs (41, 44). Axonal remodeling is regulated by synaptic transmission (37, 45, 46) and non-cell-autonomous stabilization and punishment signals (42, 43, 47). Although the precise mechanisms of axonal stabilization and punishment are not fully understood, it is likely that non-cell-autonomous signals operate at a local scale through direct cell-cell interactions or diffusible paracrine factors. Because CTB(-) non-dominant-eye sAZ synapses initially cluster around like-eye mAZ synapses and are later eliminated during eye-specific competition (Figure 3C), we hypothesized that these clustering effects may correlate with distance to the nearest neighboring eye-specific mAZ synapses.

To explore this, we first examined whether the size of CTB(-) non-dominant-eye mAZ synapses varied based on their proximity to CTB(+) dominant-eye mAZ synapses (Figure 4A/B). For each CTB(-) mAZ synapse, we measured the vesicle pool volume (Figure 4A, P4 data as an example) and AZ number (Figure 4B) as a function of each synapse's distance to the nearest CTB(+) mAZ synapse. We found no correlation between presynaptic properties and inter-eye mAZ synapse distances across all ages in both WT mice (Figure 4 A/B, left panels) and β2KO mice (Figure 4A/B, right panels) (P2/P8 data not shown). These results show that vesicle pool size and active zone number within non-dominant-eye mAZ synapses are not influenced by proximity to dominant-eye mAZ synapses.

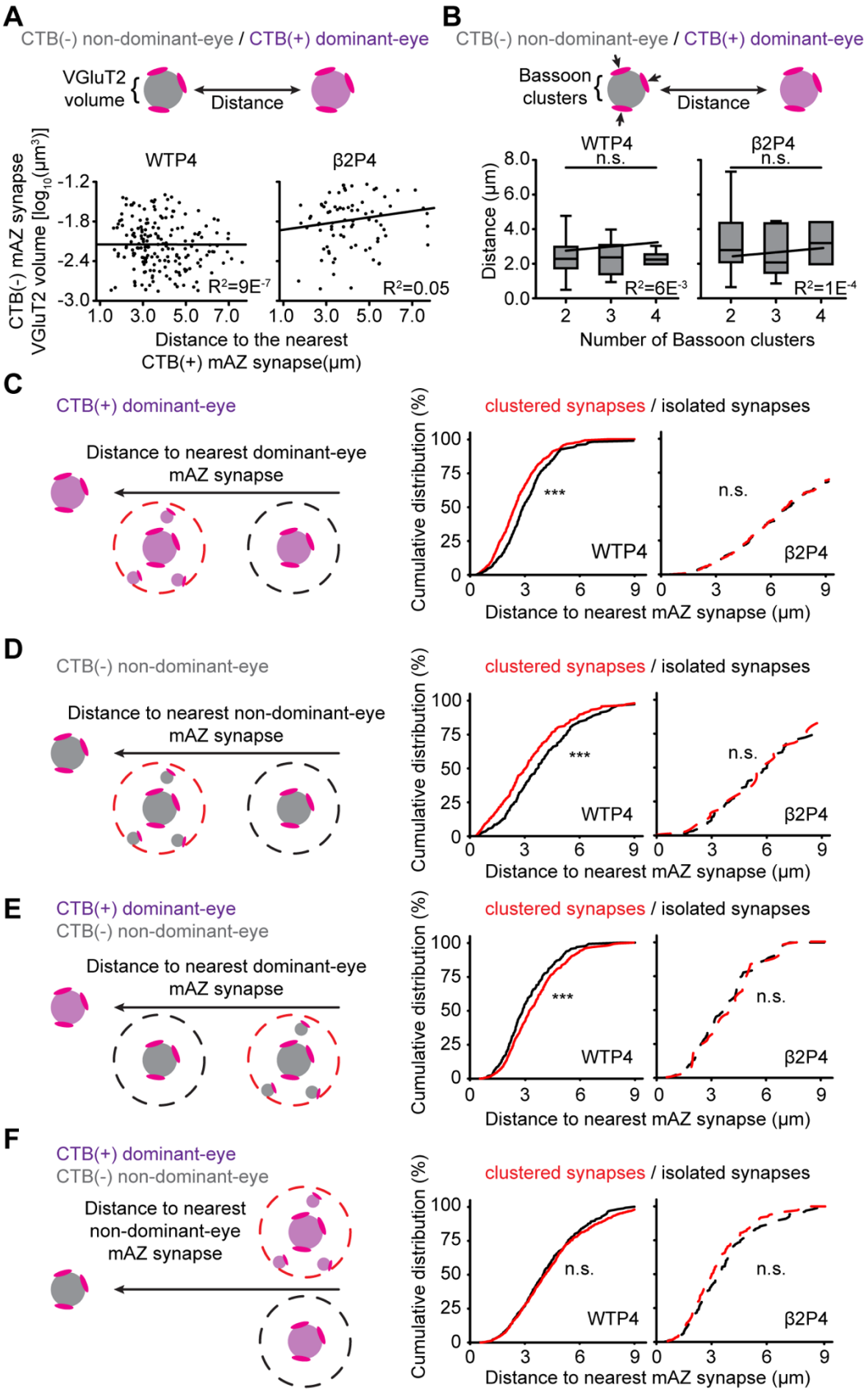

Figure 4: Synaptic clustering varies with distance to neighboring eye-specific multi-active zone synapses. (A) VGluT2 volume of CTB(-) non-dominant-eye mAZ synapses relative to their distance to the nearest CTB(+) dominant-eye mAZ synapse in a WT P4 sample (left panel) and a β2KO P4 sample (right panel). Each black dot represents one mAZ synapse. The red solid line represents the result of linear regression fitting. (B) Distributions of distances between CTB(-) non-dominant-eye mAZ synapses and their nearest CTB(+) dominant-eye mAZ synapse separated by the number of AZs within each CTB(-) mAZ synapse in WT P4 samples (left panel) and β2KO P4 samples (right panel). The median value is indicated by the horizontal line within the box, while the box boundaries represent quartile values. The whiskers represent the maximum and minimum values. A mixed model ANOVA was used to perform statistical tests. "n.s." indicates no significant differences. The red solid line represents the result of linear regression fitting. (C) Cumulative distributions of distances between CTB(+) dominant-eye mAZ synapses and their nearest CTB(+) dominant-eye mAZ synapse (cartoon) in WT P4 samples (left panel) and β2KO P4 samples (right panel). Red lines indicate clustered mAZ synapses with nearby (<1.5 μm) sAZ synapses and black lines indicate isolated mAZ synapses with no nearby sAZ synapses. (D) Same presentation as in (C), showing distances between CTB(-) mAZ synapses. (E) Same presentation as in (C), showing distances between CTB(-) non-dominant-eye mAZ synapses and their nearest CTB(+) dominant-eye mAZ synapse. (F) Same presentation as in (C), showing distances between CTB(+) dominant-eye mAZ synapses and the nearest CTB(-) non-dominant-eye mAZ synapse. For C-F, nonparametric Kolmogorov-Smirnov tests were used for statistical comparisons. "***" indicates $p<0.001$, while "n.s." indicates no significant difference from the K-S test results. Separate measurements of 5/95% confidence intervals show overlap of the two distributions in each “n.s.” instance.

313

Next, we investigated whether synaptic clustering around mAZ synapses from one eye varied based on their distance to the nearest neighboring eye-specific mAZ synapses. For this analysis, we categorized eye-specific mAZ synapses into two groups: "clustered" mAZ synapses with nearby (< 1.5 μm) sAZ synapses from the same eye, and "isolated" mAZ synapses with no nearby sAZ synapses. For the dominant-eye projection, 62-73% of all mAZ synapses were clustered (P2-P8). The mAZ ratios for the non-dominant-eye projection were 46% (P2), 51% (P4), and 54% (P8) (Figure S5). After distinguishing these two types of mAZ synapses, we measured the distance between each type and its closest mAZ synapses from each eye-of-origin (Figure 4C-F).

In WT mice at P4, CTB(+) dominant-eye clustered mAZ synapses were closer to other CTB(+) mAZ synapses compared to CTB(+) isolated mAZ synapses (Figure 4C, left panel). Similarly, CTB(-) non-dominant-eye clustered mAZ synapses were closer to the nearest CTB(-) mAZ synapse compared to CTB(-) isolated mAZ synapses (Figure 4D, left panel). These distance-dependent relationships were not observed when mAZ synapse positions of the target eye were randomized (Figure S6A/B, 5/95% confidence interval for clustered and isolated mAZ synapses: 4.40~4.60 μm and 4.44~4.60 μm from CTB(+) to CTB(+) synapses; 2.82~3.08 μm and 2.90~3.10 μm from CTB(+) to CTB(-) synapses; 4.30~4.53 μm and 4.12~4.40 μm from CTB(-) to CTB(-) synapses; 3.26~3.49 μm and 3.26~3.54 μm from CTB(-) to CTB(+) synapses). These findings indicate that synaptic clustering around a mAZ synapse is greater when it is near another mAZ synapse from the same eye. This distance-dependent clustering persisted at P8 for CTB(+) dominant-eye mAZ synapses (Figure S6C, left panel). However, at P8, CTB(-)

non-dominant-eye mAZ synapses did not show a distance-dependent clustering effect (Figure S6D, right panel). This reflected a change in the ratio of clustered/isolated CTB(-) mAZ synapses from P4-P8 (Figure S5, 5/95% confidence interval in the difference was -50.5% ~ -23.4%). Despite this shift, the density of CTB(-) mAZ synapses remained consistent (Figure 1E, 5/95% confidence interval in the difference was -0.05 ~ 0.08 synapses / μm^3).

To look for evidence of competitive interactions between synapses from the two eyes, we measured the distances between clustered and isolated CTB(-) non-dominant-eye mAZ synapses and the closest CTB(+) dominant-eye mAZ synapse (Figure 4E). In WT mice at P4, CTB(-) non-dominant-eye isolated mAZ synapses were closer to the nearest CTB(+) dominant-eye mAZ synapse compared to CTB(-) clustered mAZ synapses (Figure 4E, left panel). This effect was not observed when CTB(+) mAZ synapse positions were randomized (Figure S6A/B).

Lastly, we compared the distances between clustered and isolated CTB(+) dominant-eye mAZ synapses with respect to CTB(-) non-dominant-eye mAZ synapses and found no differences in WT mice (Figure 4F, left panel, the 5/95% confidence intervals: 3.92 ~ 4.51 μm for clustered mAZ synapses and 3.98 ~ 4.29 μm for isolated mAZ synapses). This suggests that dominant-eye synaptic clustering is not affected by proximity to non-dominant-eye mAZ synapses.

For all measured inter-synaptic relationships, distance-dependent effects on synaptic clustering were only observed in WT mice and not in β2KO mice (Figure 4 C/D, right panels; the 5/95% confidence interval for distances were 6.75 ~ 7.06 μm and 6.62 ~ 6.99 μm for clustered and isolated CTB(+) mAZ synapses, and 4.51 ~ 6.59 μm and 5.36 ~ 6.43 μm for clustered and isolated CTB (-) mAZ synapses). Together, these results show that normal spontaneous retinal activity is necessary for non-random eye-specific synaptic clustering during synaptic competition.

Discussion

Relay neurons of the dLGN function as critical integrators of locally clustered RGC inputs, which drive spike output to the primary visual cortex. In this study, we used volumetric super-resolution microscopy and eye-specific synaptic immunolabeling to show that 1) eye-specific synaptic clustering begins during retinogeniculate refinement, before eye-opening, 2)clustering occurs near RGC inputs with multiple active zones (mAZ synapses), 3)synaptic clustering depends on spontaneous retinal activity during the first postnatal week, and 4) the proximity of eye-specific mAZ synapses influences activity-dependent clustering, with nearby like-eye inputs showing increased clustering and opposite-eye inputs exhibiting reduced clustering as a function of distance to competing synapses. These results show that synaptic clustering begins at the earliest stages of eye-specific refinement and are consistent with previous studies implicating local signaling mechanisms in activity-dependent synaptic competition in the developing visual system.

Previous anatomical studies have shown that retinogeniculate glomeruli mature through the progressive clustering of RGC boutons after eye-opening in mice (10, 13, 20). These clusters form through the convergence of inputs from multiple RGCs (9-14) and by the clustering of boutons within the arbors of individual RGCs (20). The latter depends on visual experience and is partly disrupted by sensory deprivation (e.g., late dark-rearing) (20). At maturity, retinogeniculate clusters are primarily eye-specific and contain very few, weak synapses from the non-dominant eye (15, 17). Our STORM images reveal that eye-specific synaptic clustering begins before eye-opening, during the period of eye-specific competition driven by stage II cholinergic retinal waves. This clustering is characterized by the emergence of a subset of synapses containing multiple AZs (mAZ synapses), distinct from isolated RGC terminals with a single active zone (sAZ synapses). Electron microscopy images of dAPEX2-labeled RGC inputs confirmed the presence of retinogeniculate synapses with multiple active zones. Prior electron microscopy studies in the mouse found limited evidence of convergent synaptic clustering from neighboring RGCs at postnatal day 8 (10, 13), suggesting that the mAZ synapses seen in STORM images are single retinogeniculate terminals. The lack of synaptic convergence in prior EM reconstructions at P8 implies that early clustering around mAZ synapses may result from local output clustering within individual RGC arbors.

Our previous analysis of this STORM data set (25) demonstrated eye-specific differences in presynaptic vesicle pool size and vesicle association with the AZ as key factors in eye-specific competition. Here, we further identify several effects contributing

to these differences: 1) Both sAZ and mAZ synapses exhibit eye-specific differences in VGluT2 volume. By measuring VGluT2 volume near presynaptic Bassoon clusters, we found that both synapse types show eye-specific differences in VGluT2 enrichment at the AZ (Figure 2A/B), while the extent of putative vesicle docking remains similar between synapse types for each eye (Figure S7, 5/95% confidence interval for differences in VGluT2 volume near the AZ was -0.63~0.191 $\log_{10}[\mu m^3]$ for WT mice and -0.108~0.129 $\log_{10}[\mu m^3]$ for β2KO mice). 2) Dominant-eye projections form more mAZ synapses than the non-dominant-eye projections at each stage of eye-specific refinement (Figure 1F). Moreover, mAZ synapses have ~3 fold larger presynaptic vesicle pools than sAZ synapses at the peak of synaptic competition, when input densities are equivalent between the two eyes (Figure 2D). 3) On average, mAZ synapses from the dominant-eye contain more AZs per synapse compared to those from the non-dominant-eye throughout development (Figure 2C). These factors contribute to a greater eye-specific VGluT2 volume difference for mAZ synapses compared to sAZ synapses (Figure 2A/B). Since mAZ synapses are expected to have a higher release probability, they likely play an important role in driving plasticity mechanisms reliant on neurotransmission.

Indeed, mAZ synapses act as local hubs for clustering like-eye-type sAZ synapses. These clustered synapses may be formed by the same RGC axon, or by adjacent RGC axons. Our current EM data, limited to two-dimensional images, leaves open the question of whether RGC synaptic convergence or local clustering within RGC arbors is the primary contributor. Future volumetric EM reconstructions will be needed to resolve

this. Our spatial measurements from STORM images show that synaptic clustering is more likely when mAZ synapses from the same eye are closer together. This was observed for both dominant- and non-dominant-eye inputs during the peak of synaptic competition at P4 (Figure 4). Like-eye-type synaptic clustering is consistent with previous reports of non-cell-autonomous signaling mechanisms promoting eye-specific axonal stabilization (41, 42, 47). The formation of mAZ synapses may also promote clustering within individual RGC arbors, potentially through a combination of cell-intrinsic factors (e.g. elevated presynaptic calcium) and cell-cell signaling mechanisms (e.g. neurotransmission, surface delivery of transmembrane cargo) contributing to synaptic competition.

In addition to axon stabilization, competitive refinement also involves axonal retraction mediated by punishment signals. Genetic deletions of VGluT2 or RIM1 proteins in ipsilaterally-projecting RGCs decrease presynaptic vesicle release and prevent contralateral RGC axon retraction (punishment) from the ipsilateral eye-specific territory in the dLGN (37, 48). Consistent with a putative punishment mechanism, we found that non-dominant-eye mAZ synapses were less likely to be clustered if they were closer to a dominant-eye mAZ synapse. One downstream mediator of synaptic punishment is JAK2 kinase, which is phosphorylated in less active synapses (43). Similar to neurotransmission mutant phenotypes, disruption of JAK2 kinase signaling prevents axon retraction (punishment) during eye-specific competition (43).

In the adult dLGN, bouton clustering facilitates the convergence of RGC inputs representing similar visual features (e.g. direction of motion) and the integration of parallel visual channels carried by unique RGC mosaics (12, 15, 18). During development, the co-activation of neighboring RGCs by retinal waves may support the topographic refinement of clustered inputs to relay neurons. Our previous work demonstrated that abnormal retinal activity results in a significant reduction in eye-specific synapse numbers in β2KO mice (25). Additionally, β2KO mice show delayed eye-specific vesicle recruitment to the active zone by P8, a process present in WT mice as early as P2 (24). Similarly, our current analysis revealed increased vesicle pool volume and AZ number in β2KO mAZ synapses at later stages (P4 and P8) compared to WT mice (Figure 2). β2KO mice also lacked distance-dependent synaptic clustering effects until P8 (Figure S6E). Together, these results show how defects in retinal waves impact retinofugal synapse development, ultimately leading to abnormal receptive field properties (31, 49).

Although our findings support the role of non-cell autonomous signaling in synaptic competition, alternative mechanisms may also contribute to eye-specific clustering. Input targeting could be molecularly specified to produce non-random eye-specific connections with postsynaptic targets. Ipsilaterally-projecting RGCs have a distinct gene expression profile (50), which may contribute to eye-specific targeting at the synaptic level.

Our observation of synaptic clustering in the developing retinogeniculate system bears similarities to development in other circuits, such as the neuromuscular junction (NMJ). Motor neuron terminals undergo competitive refinement, where connections from a single motor axon are strengthened, while competing axons are eliminated (51-54). Synaptic competition at the NMJ is also dependent on inter-synaptic distance, with motor axons losing connections that are in closer proximity to competing synapses (51, 52). This activity-dependent process is biased toward the elimination of silenced inputs (55, 56). Interestingly, competing motor axon outputs show differences in presynaptic release probability at early stages of development, suggesting that biases in presynaptic release may underlie competition (57), possibly through the induction of local stabilization and punishment signals (54).

Although the molecular mechanisms of eye-specific retinogeniculate clustering are still unknown, our STORM imaging results provide anatomical support for local, non-cell-autonomous interactions involved in synaptic refinement. Neighboring synapses may engage in direct signaling between presynaptic RGC axon terminals or initiate postsynaptic responses that lead to retrograde signaling to stabilize or eliminate synapses based on input timing. JAK2/STAT signaling is one known mediator of synapse elimination (43), guiding future investigations into the upstream signals that regulate competition. It will also be of interest to further investigate the synapse-specific induction of synaptic tags that mediate glial-dependent pruning of weak inputs during eye-specific segregation (58-60). Future studies using dense connectomic reconstruction and cell-type-specific markers will generate valuable anatomical

snapshots of developing retinogeniculate circuits. An important goal will be to complement these anatomical resources with live nanoscopic imaging of rapid structural dynamics driving circuit refinement.

Materials and methods:

The raw imaging data in this paper were previously reported (25). Materials and methods below are adapted from this work. All Matlab and Python code used in the work is available on GitHub (https://github.com/SpeerLab). Raw STORM images of the full data are available on the open-access Brain Imaging Library (61). These images can be accessed here: https://api.brainimagelibrary.org/web/view?bildid=ace-dud-lid (WTP2A data for example). All 18 datasets are currently searchable on the BIL by keyword “dLGN” or PI last name “Speer” and a DOI for the full data set is pending.

Animals

Wild-type C57BL/6J mice (Stock Number 000664) and APEX2 mice (Stock Number 032764) used in this study were purchased from the Jackson Laboratory. ET33^{Cre} mice and β2KO were generously gifted by Drs. Eric M. Ullian (University of California, San Francisco) and Michael C. Crair (Yale School of Medicine), respectively. All experimental procedures were performed in accordance with an animal study protocol approved by the Institutional Animal Care and Use Committee (IACUC) at the University of Maryland. Neonatal male and female mice were used interchangeably for all experiments. Tissue from biological replicates (N=3 animals) was collected for each age

(P2/P4/P8) from each genotype (WT and β2KO) (18 animals total). Primers used for genotyping β2KO mice are: forward: CAGGCGTTATCCACAAAGACAGA; reverse: TTGAGGGGAGCAGAACAGAATC; mutant reverse: ACTTGGGTTTGGGCGTGTTGAG (65, 66). Primers used for genotyping ET33Cre mice are: Forward: GGTCCTTGGCAGATGGGCAT; reverse: CGGCAAACGGACAGAAGCATT.

Electron microscopy tissue preparation

Animals were deeply anesthetized with ketamine/xylazine and transcardially perfused with 5-10 mls of 37°C 0.9% sterile saline (pH 7.2) followed by 20-30 mls of 37°C 4% EM-Grade paraformaldehyde (PFA, Electron Microscopy Sciences), 2% EM-Grade glutaraldehyde (GA, Electron Microscopy Sciences), 4mM calcium chloride (CaCl2, Sigma-Aldrich) in 0.2M cacodylate buffer (pH 7.4). Brains were postfixed in the same perfusion fixative solution overnight at 4°C. Brains were sectioned in 0.2M cacodylate buffer (pH 7.4) at 100 µm using a vibratome. A circular tissue punch (~500 µm diameter) containing the dLGN was microdissected from each section using a blunt-end needle. dLGN sections were washed in 0.2M cacodylate buffer (pH 7.4) at 4°C on a rotator (4x 20 minutes). Sections were incubated in 20mM glycine (Sigma-Aldrich) in 0.2M cacodylate buffer (pH 7.4) at 4°C on a rotator for 30 minutes, followed by 5 x 20 minutes washes in 0.2M cacodylate buffer (pH 7.4) at 4°C on a rotator. dLGN sections were immersed in 0.5mg/mL DAB solution, covered with foil, for 30 minutes at 4°C on a rotator. 10 µL of 0.03% hydrogen peroxide (Sigma-Aldrich) was mixed into the DAB solution (1 mL) and incubated for 10 minutes at 4°C on a rotator (light protected). The

reaction was quenched with 0.2M cacodylate buffer (pH 7.4) washes (3 x 1-minute washes followed by 2 x 20 minutes washes).

Tissue preparation for scanning electron microscopy

dLGN sections were fixed in 2% osmium tetroxide (Electron Microscopy Sciences) in 0.15M cacodylate buffer (pH 7.4) for 45 minutes at room temperature. Sections were reduced with 2.5% potassium ferricyanide (Electron Microscopy Sciences) in 0.15M cacodylate buffer (pH 7.4) for 45 minutes at room temperature in the dark, followed by 2 x 10-minute washes in double distilled water. Sections were incubated in 1% aqueous thiocarbohydrazide (Electron Microscopy Sciences) for 20 minutes, followed by 2 x 10-minute washes in double distilled water. Samples were fixed in 1% aqueous osmium tetroxide for 45 minutes at room temperature, followed by 2 x 10-minute washes in double distilled water. Sections were postfixed in 1% uranyl acetate (Electron Microscopy Sciences) in 25% ethanol in the dark for 20 minutes at room temperature and washed and stored in double distilled water overnight. The next day, samples were stained with aqueous lead aspartate at 60°C for 30 minutes and washed with double distilled water 2 x 10 minutes. Tissues were dehydrated in a graded dilution series of 100% ethanol (35%; 50%; 70%; 95%; 100%; 100%; 100% EtOH) for 10 minutes each at room temperature. Samples were immersed in propylene oxide (Electron Microscopy Sciences) 3 x 10 minutes at room temperature, followed by a series of epon resin/propylene oxide (812 Epon Resin, Electron Microscopy Sciences) exchanges with increasing resin concentrations (50% resin/50% propylene oxide; 65% resin/35% propylene oxide; 75% resin/25% propylene oxide; 100% resin; 100% resin) for 90

563 minutes each. Tissues were transferred to BEEM capsules (Electron Microscopy
564 Sciences) that were filled with 100% resin and polymerized for at least 48 hours at
565 60°C.
566

567 Transmission electron microscopy image acquisition

568 Plasticized sections were cut at 70 nm with a Histo Jumbo diamond knife (DiATOME)
569 using a Leica UC7 ultramicrotome. Sections were decompressed using chloroform
570 vapor and collected onto 3.05mm 200 mesh Gilder thin bar hexagonal mesh copper
571 grids (T200H-Cu, Electron Microscopy Sciences). Sections were imaged unstained on a
572 Hitachi HT7700 transmission electron microscope (HT7700, Hitachi High-Tech America,
573 Inc.) at 80kV.
574

575 Eye injections

576 Intraocular eye injections were performed one day before tissue collection. Briefly, mice
577 were anesthetized by inhalant isoflurane and sterile surgical spring scissors were used
578 to gently part the eyelid to expose the corneoscleral junction. A small hole was made in
579 the eye using a sterile 34-gauge needle and ~0.5 µL of cholera toxin subunit B
580 conjugated with Alexa Fluor 488 (CTB-488, ThermoFisher Scientific, Catalogue
581 Number: C34775) diluted in 0.9% sterile saline was intravitreally pressure-injected into
582 the right eye using a pulled-glass micropipette coupled to a Picospritzer (Parker
583 Hannifin).
584

585 dLGN tissue preparation for STORM imaging

Animals were deeply anesthetized with ketamine/xylazine and transcardially perfused with 5-10 mls of 37°C 0.9% sterile saline followed by 10 mls of room temperature 4% EM-Grade paraformaldehyde (PFA, Electron Microscopy Sciences) in 0.9% saline. Brains were embedded in 2.5% agarose and sectioned in the coronal plane at 100 µm using a vibratome. From the full anterior-posterior series of dLGN sections (~6-8 sections) we selected the central two sections for staining in all biological replicates. These sections were morphologically consistent with Figures 134-136 (5.07-5.31 mm) of the postnatal day 6 mouse brain from Paxinos, et al., “Atlas of the developing mouse brain” Academic Press, 2020 (62). Selected sections were postfixed in 4% PFA for 30 minutes at room temperature and then washed for 30-40 minutes in 1X PBS. The dLGN was identified by the presence of CTB-488 signals using a fluorescence dissecting microscope. A circular tissue punch (~500 µm diameter) containing the dLGN was microdissected from each section using a blunt-end needle. A small microknife cut was made at the dorsal edge of the dLGN which, together with the CTB-488 signal, enabled us to identify the dLGN orientation during image acquisition.

Immunohistochemistry

We used a serial-section single-molecule localization imaging approach to prepare samples and collect super-resolution fluorescence imaging volumes as previously described (26). dLGN tissue punches were blocked in 10% normal donkey serum (Jackson ImmunoResearch, Catalogue Number: 017-000-121) with 0.3% Triton X-100 (Sigma-Aldrich Inc.) and 0.02% sodium azide (Sigma-Aldrich Inc.) diluted in 1X PBS for 2-3 hours at room temperature and then incubated in primary antibodies for ~72 hours

609 at 4°C. Primary antibodies used were Rabbit anti-Homer1 (Synaptic Systems,
610 Catalogue Number: 160003, 1:100) to label postsynaptic densities (PSDs), mouse anti-
611 Bassoon (Abcam, Catalogue Number AB82958, 1:100) to label presynaptic active
612 zones (AZs), and guinea pig anti-VGluT2 (Millipore, Catalogue Number AB251-I, 1:100)
613 to label presynaptic vesicles. Following primary antibody incubation, tissues were
614 washed in 1X PBS for 6 x 20 minutes at room temperature and incubated in secondary
615 antibody solution overnight for ~36 hours at 4°C. The secondary antibodies used were
616 donkey anti-rabbit IgG (Jackson ImmunoResearch, Catalogue Number 711-005-152,
617 1:100) conjugated with Dy749P1 (Dyomics, Catalogue Number 749P1-01) and Alexa
618 Fluor 405 (ThermoFisher, Catalogue Number: A30000), donkey anti-mouse IgG
619 (Jackson ImmunoResearch, Catalogue Number 715-005-150, 1:100) conjugated with
620 Alexa Fluor 647 (ThermoFisher, Catalogue Number: A20006) and Alexa Fluor 405, and
621 donkey anti-guinea pig IgG (Jackson ImmunoResearch, Catalogue Number 706-005-
622 148, 1:100) conjugated with Cy3b (Cytiva, Catalogue Number: PA63101). Tissues were
623 washed 6 x 20 minutes in 1X PBS at room temperature after secondary antibody
624 incubation.
625

626 Postfixation, dehydration, and embedding in epoxy resin

627 Tissue embedding was performed as previously described (26). Tissues were postfixed
628 with 3% PFA + 0.1% GA (Electron Microscopy Sciences) in PBS for 2 hours at room
629 temperature and then washed in 1X PBS for 20 minutes. To plasticize the tissues for
630 ultrasectioning, the tissues were first dehydrated in a graded dilution series of 100%
631 ethanol (50%/70%/90%/100%/100% EtOH) for 15 minutes each at room temperature

and then immersed in a series of epoxy resin/100% EtOH exchanges (Electron Microscopy Sciences) with increasing resin concentration (25% resin/75% ethanol; 50% resin/50% ethanol; 75% resin/25% ethanol; 100% resin; 100% resin) for 2 hours each. Tissues were transferred to BEEM capsules (Electron Microscopy Sciences) that were filled with 100% resin and polymerized for 16 hours at 70°C.

Ultrasectioning

Plasticized tissue sections were cut using a Leica UC7 ultramicrotome at 70 nm using a Histo Jumbo diamond knife (DiATOME). Chloroform vapor was used to reduce compression after cutting. For each sample, ~100 sections were collected on a coverslip coated with 0.5% gelatin and 0.05% chromium potassium (Sigma-Aldrich Inc.), dried at 60 degrees for 25 minutes, and protected from light prior to imaging.

Imaging chamber preparation

Coverslips were chemically etched in 10% sodium ethoxide for 5 minutes at room temperature to remove the epoxy resin and expose the dyes to the imaging buffer for optimal photoswitching. Coverslips were then rinsed with ethanol and dH_2O. To create fiducial beads for flat-field and chromatic corrections, we mixed 715/755nm and 540/560nm, carboxylate-modified microspheres (Invitrogen, Catalogue Numbers F8799 and F8809, 1:8 ratio respectively) to create a high-density fiducial marker and then further diluted the mixture at 1:750 with Dulbecco's PBS to create a low-density bead solution. Both high- and low-density bead solutions were spotted on the coverslip (~0.7 µL each) for flat-field and chromatic aberration correction respectively. Excess beads

were rinsed away with dH2O for 1-2 minutes. The coverslip was attached to a glass slide with double-sided tape to form an imaging chamber. The chamber was filled with STORM imaging buffer (10% glucose, 17.5μM glucose oxidase, 708nM catalase, 10mM MEA, 10mM NaCl, and 200mM Tris) and sealed with epoxy.

Imaging setup

Imaging was performed using a custom single-molecule super-resolution imaging system. The microscope contained low (4x/10x air) and high (60x 1.4NA oil immersion) magnitude objectives mounted on a commercial frame (Nikon Ti-U) with back optics arranged for oblique incident angle illumination. We used continuous-wave lasers at 488nm (Coherent), 561nm (MPB), 647nm (MPB), and 750nm (MPB) to excite Alexa 488, Cy3B, Alexa 647, and Dy749P1 dyes respectively. A 405 nm cube laser (Coherent) was used to reactivate Dy749P1 and Alexa647 dye photoswitching. The microscope was fitted with a custom pentaband/pentanotch dichroic filter set and a motorized emission filter wheel. The microscope also contained an IR laser-based focus lock system to maintain optimal focus during automatic image acquisition. Images were collected on 640*640-pixel region of an sCMOS camera (ORCA-Flash4.0 V3, Hamamatsu Photonics) with a pixel size of ~155 nm.

Automated image acquisition

Fiducials and tissue sections on the coverslip were imaged using the low magnification objective (4X) to create a mosaic overview of the specimen. Beads/sections were then imaged at high magnification (60X) to select regions of interest (ROIs) in the Cy3B and

Alexa 488 channels. Before final image acquisition, laser intensities and the incident angle were adjusted to optimize photoswitching for STORM imaging and utilize the full dynamic range of the camera for conventional imaging.

Low-density bead images were taken in 16 partially overlapping ROIs. 715/755nm beads were excited using 750 nm light and images were collected through Dy749P1 and Alexa 647 emission filters. 540/560nm beads were excited using a 488 nm laser and images were collected through Alexa 647, Cy3B, and Alexa 488 emission filters. These fiducial images were later used to generate a non-linear warping transform to correct chromatic aberration. Next, ROIs within each tissue section were imaged at conventional (diffraction-limited) resolution in all four-color channels sequentially.

Following conventional image acquisition, a partially overlapping series of 9 images were collected in the high-density bead field for all 4 channels (Dy749P1, Alexa 647, Cy3B, and Alexa 488). These images were later used to perform a flat-field image correction of non-uniform laser illumination across the ROIs. Another round of bead images was taken as described above in a different ROI of the low-density bead field. These images were later used to confirm the stability of chromatic offsets during imaging. All ROIs within physical sections were then imaged by STORM for Dy749P1 and Alexa 647 channels. Images were acquired using a custom progression of increasing 405nm laser intensity to control single-molecule switching. 8000 frames of Dy749P1 channel images were collected (60 Hz imaging) followed by 12000 frames of

Alexa 647 channel images (100 Hz). In a second imaging pass, the same ROIs were imaged for Cy3B and Alexa 488 channels, each for 8000 frames (60 Hz).

We imaged the ipsilateral and contralateral ROIs separately in each physical section of the dLGN. For consistency of ROI selection across biological replicates at each age, we identified the dorsal-ventral (DV) axis of the dLGN and selected ROIs within the center (core region) at 2/5 (ipsilateral ROI) and 4/5 (contralateral ROI) of the full DV length.

Image processing

Single-molecule localization was performed using a previously described DAOSTORM algorithm (63) modified for use with sCMOS cameras (64). Molecule lists were rendered as 8-bit images with 15.5 nm pixel size where each molecule is plotted as an intensity distribution with an area reflecting its localization precision. Low-density fiducial images were used for chromatic aberration correction. We localized 715/755 beads in Dy749P1 and Alexa 647 channels, and 540/560 beads in Alexa 647, Cy3B, and Alexa 488 channels. A third-order polynomial transform map was generated by matching the positions of each bead in all channels to the Alexa 647 channel. The average residual error of bead matching was <15 nm for all channels. The transform maps were applied to both 4-color conventional and STORM images. Conventional images were upscaled (by 10X) to match the STORM image size. The method to align serial sections was previously described (25). STORM images were first aligned to their corresponding conventional images by image correlation. To generate an aligned 3D image stack from serial sections, we normalized the intensity of all Alexa 488 images and used these

723 normalized images to generate both rigid and elastic transformation matrices for all four-
724 color channels of both STORM and conventional data. The final image stack was then
725 rotated and cropped to exclude incompletely imaged edge areas. To further confirm that
726 the processed region corresponds to the contralateral dLGN, conventional CTB(+)
727 signals of the labeled contralateral projection were thresholded to create a polygonal
728 mask (a convex hull analysis linking the outermost CTB signals in the image volume).
729 The mask was then applied to STORM images to exclude peripheral areas where CTB
730 signals were absent or faint.
731

732 Cell body filter

733 The aligned STORM images had non-specific labeling of cell bodies in Dy749P1 and
734 Alexa 647 channels corresponding to Homer1 and Bassoon immunolabels. To limit
735 synaptic cluster identification to the neuropil region we identified cell bodies based on
736 their Dy749P1 signal and excluded these regions from further image processing.
737 STORM images were convolved with a Gaussian function (σ=140 nm) and then
738 binarized using the lower threshold of a two-level Otsu threshold method. We located
739 connected components in the thresholded images and generated a mask based on
740 components larger than e^{11} voxels. Because cell body clusters were orders of
741 magnitude larger than synaptic clusters, the cell body filter algorithm was robust to a
742 range of size thresholds. The mask was applied to images of all channels to exclude
743 cell body areas.
744

745 Eye-specific synapse identification and quantification

To correct for minor variance in image intensity across physical sections, we normalized the pixel intensity histogram of each section to the average histogram of all sections. Image histograms were rescaled to make full use of the 8-bit range. Using a two-level Otsu threshold method, the conventional images were thresholded into three classes: a low-intensity background, low-intensity signals above the background representing non-synaptic labeling, and high-intensity signals representing synaptic structures. The conventional images were binarized by the lower two-level Otsu threshold, generating a mask for STORM images to filter out background signals. STORM images were convolved with a Gaussian function (σ= 77.5 nm) and thresholded using the higher two-level Otsu threshold. Following thresholding, connected components were identified in three dimensions using MATLAB 'conncomp' function. A watershedding approach was applied to split large clusters that were improperly connected. Clusters were kept for further analysis only if they contained aligned image information across two or more physical sections. We also removed all edge synapses from our analysis by excluding synapses that did not have blank image data on all adjacent sides.

To distinguish non-specific immunolabeling from true synaptic signals, we quantified two parameters for each cluster: cluster volume and cluster signal density calculated by the ratio of within-cluster pixels with positive signal intensity in the raw STORM images. Two separate populations were identified in 2D histograms plotted from these two parameters. We manually selected the population with higher volumes and signal densities representing synaptic structures. To test the robustness of the manual

768 selection, we performed multiple repeated measurements of the same data and
769 discovered a between-measurement variance of <1% (data not shown).
770
771 To identify paired pre- and postsynaptic clusters, we first measured the centroid-
772 centroid distance of each cluster in the Dy749P1 (Homer1) and Alexa 647 (Bassoon)
773 channels to the closest cluster in the other channel. We next quantified the signal
774 intensity of each opposing synaptic channel within a 140 nm shell surrounding each
775 cluster. A 2D histogram was plotted based on the measured centroid-centroid distances
776 and opposing channel signal densities of each cluster. Paired clusters with closely
777 positioned centroids and high intensities of apposed channel signal were identified
778 using the OPTICS algorithm. In total we identified 49,414 synapses from WT samples (3
779 samples each at P2/P4/P8, 9 total samples) and 33,478 synapses in $\beta2^{-/-}$ mutants (3
780 samples each at P2/P4/P8, 9 total samples). Retinogeniculate synapses were identified
781 by pairing Bassoon (Alexa 647) clusters with VGluT2 (Cy3B) clusters using the same
782 method as pre/post-synaptic pairing. Synapses from the right eye were identified by
783 pairing VGluT2 clusters with CTB (Alexa 488) clusters. The volume of each cluster
784 reflected the total voxel volume of all connected voxels, and the total signal intensity
785 was a sum of voxel intensity within the volume of the connected voxels.
786

787 Multi-AZ synapse identification and quantification

788 To determine whether an eye-specific VGluT2 cluster is a mAZ synapse or a sAZ
789 synapse, we measured the number of active zones (defined by individual Bassoon
790 clusters) associated with each VGluT2 cluster in the dataset. A 3D shell was extended

140 nm from the surface voxels of each VGluT2 cluster and any Bassoon clusters that fell within the shell were considered to be associated with the target VGluT2 cluster. The number of active zones (AZs) associated with each VGluT2 cluster was then measured. VGluT2 clusters associated with more than 1 AZ were defined as mAZ synapses, while those associated with only 1 AZ were defined as sAZ synapses.

Quantification of mAZ and sAZ synapse VGluT2 cluster volume was performed using the "regionprops" function in MATLAB, which provided the voxel size and weighted centroid of each VGluT2 cluster. The search for sAZ synapses adjacent to mAZ synapses (synaptic clustering analysis) was conducted using a similar search approach as for associated Bassoon clusters, with expansion shell sizes ranging from 1 μm to 4 μm from the surface voxels of each mAZ synapse. The main figures in the study utilized an expansion size of 1.5 μm. An eye-specific sAZ synapse was considered to be near a mAZ synapse if its weighted centroid fell within the expanded region.

Quantification and statistical analysis

Statistical analysis was performed using SPSS. Plots were generated by SPSS or R (ggplot2). Statistical details are presented in the figure legends. For all measurements in this paper, we analyzed N = 3 biological replicates (individual mice) for each genotype (WT and β2KO) at each age (P2, P4, and P8). Cluster densities, synapse AZ number, average VGluT2 cluster volume, and all fractional measurements were presented as mean ± SEM values in paired bar graphs and statistical analysis was performed using paired-T tests. Nonparametric Kolmogorov-Smirnov tests were used in all cumulative

814 histogram comparisons. We used a linear mixed model to compare VGluT2 cluster
815 volumes (Figure 2) and the distance measurements in Figure 4B. For VGluT2 cluster
816 volume comparisons, the age or eye-of-origin was the fixed main factor and biological
817 replicate IDs were nested random factors. In distance measurement comparisons, the
818 mAZ synapse AZ number was the fixed main factor and biological replicate IDs were
819 nested random factors. In violin plots, each violin showed the distribution of grouped
820 data from all biological replicates from the same condition. Each black dot represents
821 the median value of each biological replicate, and the horizontal black line represents
822 the group median. Black lines connect measurements of CTB(+) and CTB(-)
823 populations from the same biological replicate. Asterisks in all figures indicate statistical
824 significance: *P<0.05, **P<0.01, ***P<0.001. For VGluT2 volume comparisons, we
825 calculated 5/95% confidence intervals based on the mixed linear model. 5/95%
826 confidence intervals in synapse densities, AZ numbers, and distances were calculated
827 for paired or unpaired data comparisons using SPSS.
828

829 # Acknowledgements:

830 We thank Drs. Michael C. Crair (Yale University) and Eric M. Ullian (University of
831 California, San Francisco) for generously sharing the β2KO and ET33^{Cre} mouse lines
832 used in this work. We are grateful to Tim Maugel in the Laboratory for Biological
833 Ultrastructure (UMD) for his assistance with transmission electron microscopy
834 experiments. The research was funded by National Institutes of Health
835 grant DP2MH125812 (C.M.S.).
836

Author contributions:

Conceptualization, C.Z. and C.M.S.; data curation, C.Z., T.V., C.M.S.; formal analysis, C.Z. and C.M.S.; funding acquisition, C.M.S.; investigation, C.Z., T.V., C.M.S.; methodology, C.Z., T.V., C.M.S.; project administration, C.Z. and C.M.S.; resources, C.Z., T.V., C.M.S.; software, C.Z. and C.M.S.; supervision, C.M.S.; validation, C.Z., T.V., C.M.S.; visualization, C.Z., T.V., C.M.S.; writing – original draft preparation, C.Z. and C.M.S.; writing – review & editing, C.Z., T.V., C.M.S.

References:

1. Rall W. Electrophysiology of a dendritic neuron model. Biophys J. 1962;2(2 Pt 2):145-67.
2. Mel B, editor The Clusteron: Toward a Simple Abstraction for a Complex Neuron1991 1991: Morgan-Kaufmann.
3. Poirazi P, Mel BW. Impact of active dendrites and structural plasticity on the memory capacity of neural tissue. Neuron. 2001;29(3):779-96.
4. Mel BW, Schiller J, Poirazi P. Synaptic plasticity in dendrites: complications and coping strategies. Curr Opin Neurobiol. 2017;43:177-86.
5. Leighton AH, Lohmann C. The Wiring of Developing Sensory Circuits-From Patterned Spontaneous Activity to Synaptic Plasticity Mechanisms. Front Neural Circuits. 2016;10:71.
6. Winnubst J, Lohmann C. Synaptic clustering during development and learning: the why, when, and how. Front Mol Neurosci. 2012;5:70.
7. Kastellakis G, Poirazi P. Synaptic Clustering and Memory Formation. Front Mol Neurosci. 2019;12:300.
8. Kirchner JH, Gjorgjieva J. Emergence of synaptic organization and computation in dendrites. 2022;28(1):21-30.
9. Bickford ME. Synaptic organization of the dorsal lateral geniculate nucleus. Eur J Neurosci. 2019;49(7):938-47.
10. Bickford ME, Slusarczyk A, Dilger EK, Krahe TE, Kucuk C, Guido W. Synaptic development of the mouse dorsal lateral geniculate nucleus. J Comp Neurol. 2010;518(5):622-35.
11. Hammer S, Monavarfeshani A, Lemon T, Su J, Fox MA. Multiple Retinal Axons Converge onto Relay Cells in the Adult Mouse Thalamus. Cell Rep. 2015;12(10):1575-83.
12. Morgan JL, Berger DR, Wetzel AW, Lichtman JW. The Fuzzy Logic of Network Connectivity in Mouse Visual Thalamus. Cell. 2016;165(1):192-206.
13. Monavarfeshani A, Stanton G, Van Name J, Su K, Mills WA, 3rd, Swilling K, et al. LRRTM1 underlies synaptic convergence in visual thalamus. Elife. 2018;7.
14. Hammer S, Carrillo GL, Govindaiah G, Monavarfeshani A, Bircher JS, Su J, et al. Nuclei-specific differences in nerve terminal distribution, morphology, and development in mouse visual thalamus. Neural Dev. 2014;9:16.
15. Rompani SB, Mullner FE, Wanner A, Zhang C, Roth CN, Yonehara K, et al. Different Modes of Visual Integration in the Lateral Geniculate Nucleus Revealed by Single-Cell-Initiated Transsynaptic Tracing. Neuron. 2017;93(4):767-76 e6.
16. Litvina EY, Chen C. Functional Convergence at the Retinogeniculate Synapse. Neuron. 2017;96(2):330-8 e5.
17. Bauer J, Weiler S, Fernholz MHP, Laubender D, Scheuss V, Hubener M, et al. Limited functional convergence of eye-specific inputs in the retinogeniculate pathway of the mouse. Neuron. 2021;109(15):2457-68 e12.
18. Liang L, Fratzl A, Goldey G, Ramesh RN, Sugden AU, Morgan JL, et al. A Fine-Scale Functional Logic to Convergence from Retina to Thalamus. Cell. 2018;173(6):1343-55 e24.
19. Pulikkottil VV, Somashekar BP, Bhalla US. Computation, wiring, and plasticity in synaptic clusters. Curr Opin Neurobiol. 2021;70:101-12.

20. Hong YK, Park S, Litvina EY, Morales J, Sanes JR, Chen C. Refinement of the retinogeniculate synapse by bouton clustering. Neuron. 2014;84(2):332-9.
21. Muir-Robinson G, Hwang BJ, Feller MB. Retinogeniculate axons undergo eye-specific segregation in the absence of eye-specific layers. J Neurosci. 2002;22(13):5259-64.
22. Godement P, Salaün J, Imbert M. Prenatal and postnatal development of retinogeniculate and retinocollicular projections in the mouse. J Comp Neurol. 1984;230(4):552-75.
23. Jaubert-Miazza L, Green E, Lo FS, Bui K, Mills J, Guido W. Structural and functional composition of the developing retinogeniculate pathway in the mouse. Vis Neurosci. 2005;22(5):661-76.
24. Butts DA, Kanold PO, Shatz CJ. A burst-based "Hebbian" learning rule at retinogeniculate synapses links retinal waves to activity-dependent refinement. PLoS Biol. 2007;5(3):e61.
25. Zhang C, Yadav S, Speer CM. The synaptic basis of activity-dependent eye-specific competition. Cell Rep. 2023;42(2):112085.
26. Vatan T, Minehart JA, Zhang C, Agarwal V, Yang J, Speer CM. Volumetric super-resolution imaging by serial ultrasectioning and stochastic optical reconstruction microscopy in mouse neural tissue. STAR Protocols. 2021;2(4):100971.
27. Xu HP, Burbridge TJ, Chen MG, Ge X, Zhang Y, Zhou ZJ, et al. Spatial pattern of spontaneous retinal waves instructs retinotopic map refinement more than activity frequency. Dev Neurobiol. 2015;75(6):621-40.
28. Xu HP, Burbridge TJ, Ye M, Chen M, Ge X, Zhou ZJ, et al. Retinal Wave Patterns Are Governed by Mutual Excitation among Starburst Amacrine Cells and Drive the Refinement and Maintenance of Visual Circuits. J Neurosci. 2016;36(13):3871-86.
29. Xu HP, Furman M, Mineur YS, Chen H, King SL, Zenisek D, et al. An instructive role for patterned spontaneous retinal activity in mouse visual map development. Neuron. 2011;70(6):1115-27.
30. Rossi FM, Pizzorusso T, Porciatti V, Marubio LM, Maffei L, Changeux JP. Requirement of the nicotinic acetylcholine receptor beta 2 subunit for the anatomical and functional development of the visual system. Proc Natl Acad Sci U S A. 2001;98(11):6453-8.
31. Grubb MS, Rossi FM, Changeux J-P, Thompson ID. Abnormal Functional Organization in the Dorsal Lateral Geniculate Nucleus of Mice Lacking the β2 Subunit of the Nicotinic Acetylcholine Receptor. Neuron. 2003;40(6):1161-72.
32. Dhande OS, Hua EW, Guh E, Yeh J, Bhatt S, Zhang Y, et al. Development of single retinofugal axon arbors in normal and beta2 knock-out mice. J Neurosci. 2011;31(9):3384-99.
33. Sun C, Warland DK, Ballesteros JM, van der List D, Chalupa LM. Retinal waves in mice lacking the beta2 subunit of the nicotinic acetylcholine receptor. Proc Natl Acad Sci U S A. 2008;105(36):13638-43.
34. Stafford BK, Sher A, Litke AM, Feldheim DA. Spatial-temporal patterns of retinal waves underlying activity-dependent refinement of retinofugal projections. Neuron. 2009;64(2):200-12.
35. Bansal A, Singer JH, Hwang BJ, Xu W, Beaudet A, Feller MB. Mice lacking specific nicotinic acetylcholine receptor subunits exhibit dramatically altered spontaneous activity patterns and reveal a limited role for retinal waves in forming ON and OFF circuits in the inner retina. J Neurosci. 2000;20(20):7672-81.

940 36. Zhang Q, Lee WA, Paul DL, Ginty DD. Multiplexed peroxidase-based electron microscopy
941 labeling enables simultaneous visualization of multiple cell types. Nat Neurosci. 2019;22(5):828-
942 39.
943 37. Koch SM, Dela Cruz CG, Hnasko TS, Edwards RH, Huberman AD, Ullian EM. Pathway-
944 specific genetic attenuation of glutamate release alters select features of competition-based
945 visual circuit refinement. Neuron. 2011;71(2):235-42.
946 38. Assali A, Gaspar P, Rebsam A. Activity dependent mechanisms of visual map formation--
947 from retinal waves to molecular regulators. Semin Cell Dev Biol. 2014;35:136-46.
948 39. Fassier C, Nicol X. Retinal Axon Interplay for Binocular Mapping. Front Neural Circuits.
949 2021;15:679440.
950 40. Faust TE, Gunner G, Schafer DP. Mechanisms governing activity-dependent synaptic
951 pruning in the developing mammalian CNS. Nat Rev Neurosci. 2021;22(11):657-73.
952 41. Rahman TN, Munz M, Kutsarova E, Bilash OM, Ruthazer ES. Stentian structural plasticity
953 in the developing visual system. Proc Natl Acad Sci U S A. 2020;117(20):10636-8.
954 42. Louail A, Sierksma MC, Chaffiol A, Baudet S, Assali A, Couvet S, et al. cAMP-Dependent
955 Co-stabilization of Axonal Arbors from Adjacent Developing Neurons. Cell Rep.
956 2020;33(1):108220.
957 43. Yasuda M, Nagappan-Chettiar S, Johnson-Venkatesh EM, Umemori H. An activity-
958 dependent determinant of synapse elimination in the mammalian brain. Neuron.
959 2021;109(8):1333-49 e6.
960 44. Munz M, Gobert D, Schohl A, Poquérusse J, Podgorski K, Spratt P, et al. Rapid Hebbian
961 axonal remodeling mediated by visual stimulation. Science. 2014;344(6186):904-9.
962 45. Fredj NB, Hammond S, Otsuna H, Chien C-B, Burrone J, Meyer MP. Synaptic Activity and
963 Activity-Dependent Competition Regulates Axon Arbor Maturation, Growth Arrest, and
964 Territory in the Retinotectal Projection. J Neurosci. 2010;30(32):10939.
965 46. Hua JY, Smear MC, Baier H, Smith SJ. Regulation of axon growth in vivo by activity-based
966 competition. Nature. 2005;434(7036):1022-6.
967 47. Kutsarova E, Schohl A, Munz M, Wang A, Zhang YY, Bilash OM, et al. BDNF signaling in
968 correlation-dependent structural plasticity in the developing visual system. PLoS Biol.
969 2023;21(4):e3002070.
970 48. Assali A, Le Magueresse C, Bennis M, Nicol X, Gaspar P, Rebsam A. RIM1/2 in retinal
971 ganglion cells are required for the refinement of ipsilateral axons and eye-specific segregation.
972 Sci Rep. 2017;7(1):3236.
973 49. Ge X, Zhang K, Gribizis A, Hamodi AS, Sabino AM, Crair MC. Retinal waves prime visual
974 motion detection by simulating future optic flow. Science. 2021;373(6553).
975 50. Fernández-Nogales M, López-Cascales MT, Murcia-Belmonte V, Escalante A, Fernández-
976 Albert J, Muñoz-Viana R, et al. Multiomic Analysis of Neurons with Divergent Projection
977 Patterns Identifies Novel Regulators of Axon Pathfinding. Adv Sci (Weinh).
978 2022;9(29):e2200615.
979 51. Balice-Gordon RJ, Chua CK, Nelson CC, Lichtman JW. Gradual loss of synaptic cartels
980 precedes axon withdrawal at developing neuromuscular junctions. Neuron. 1993;11(5):801-15.
981 52. Gan WB, Lichtman JW. Synaptic segregation at the developing neuromuscular junction.
982 Science. 1998;282(5393):1508-11.

53. Wyatt RM, Balice-Gordon RJ. Activity-dependent elimination of neuromuscular synapses. J Neurocytol. 2003;32(5-8):777-94.
54. Sanes JR, Lichtman JW. Development of the vertebrate neuromuscular junction. Annu Rev Neurosci. 1999;22:389-442.
55. Buffelli M, Burgess RW, Feng G, Lobe CG, Lichtman JW, Sanes JR. Genetic evidence that relative synaptic efficacy biases the outcome of synaptic competition. Nature. 2003;424(6947):430-4.
56. Balice-Gordon RJ, Lichtman JW. Long-term synapse loss induced by focal blockade of postsynaptic receptors. Nature. 1994;372(6506):519-24.
57. Kopp DM, Perkel DJ, Balice-Gordon RJ. Disparity in neurotransmitter release probability among competing inputs during neuromuscular synapse elimination. J Neurosci. 2000;20(23):8771-9.
58. Chung WS, Clarke LE, Wang GX, Stafford BK, Sher A, Chakraborty C, et al. Astrocytes mediate synapse elimination through MEGF10 and MERTK pathways. Nature. 2013;504(7480):394-400.
59. Stevens B, Allen NJ, Vazquez LE, Howell GR, Christopherson KS, Nouri N, et al. The classical complement cascade mediates CNS synapse elimination. Cell. 2007;131(6):1164-78.
60. Schafer DP, Lehrman EK, Kautzman AG, Koyama R, Mardinly AR, Yamasaki R, et al. Microglia sculpt postnatal neural circuits in an activity and complement-dependent manner. Neuron. 2012;74(4):691-705.
61. Benninger K, Hood G, Simmel D, Tuite L, Wetzel A, Ropelewski A, et al. Cyberinfrastructure of a Multi-Petabyte Microscopy Resource for Neuroscience Research. Practice and Experience in Advanced Research Computing; Portland, OR, USA: Association for Computing Machinery; 2020. p. 1–7.
62. Paxinos G. Atlas of the developing mouse brain at E17.5, P0 and P6. 1st ed. Amsterdam ; Boston: Elsevier; 2007. xi, 353 p. p.
63. Babcock H, Sigal YM, Zhuang X. A high-density 3D localization algorithm for stochastic optical reconstruction microscopy. Optical Nanoscopy. 2012;1(6).
64. Babcock HP, Huang F, Speer CM. Correcting Artifacts in Single Molecule Localization Microscopy Analysis Arising from Pixel Quantum Efficiency Differences in sCMOS Cameras. Sci Rep. 2019;9(1):18058.

Supporting information:

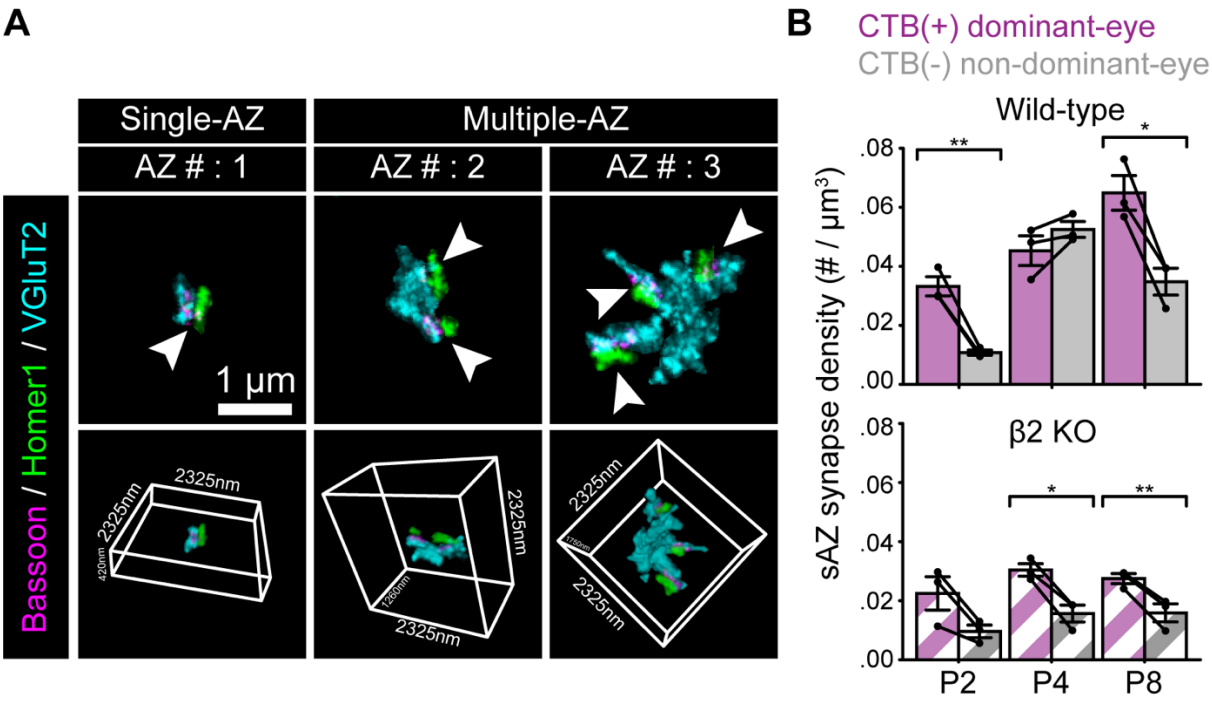

Figure S1: Eye-specific differences in sAZ synapse density in the first postnatal week, related to Figure 1. (A) Representative sAZ (left panels) and mAZ (middle and right panels) synapses (maximum projection images, top panels) and their 3D renderings (bottom panels). Arrowheads point to individual active zones. (B) The density of eye-specific sAZ synapses across ages in WT (top panel) and β2KO mice (bottom panel). Error bars represent means ± SEMs (N=3 biological replicates for each age/genotype). Black dots represent mean values from separate biological replicates and black lines connect measurements within each replicate. Statistical significance between eye-specific synapse measurements was assessed using paired T-tests. *: P<0.05. **: p<0.01.

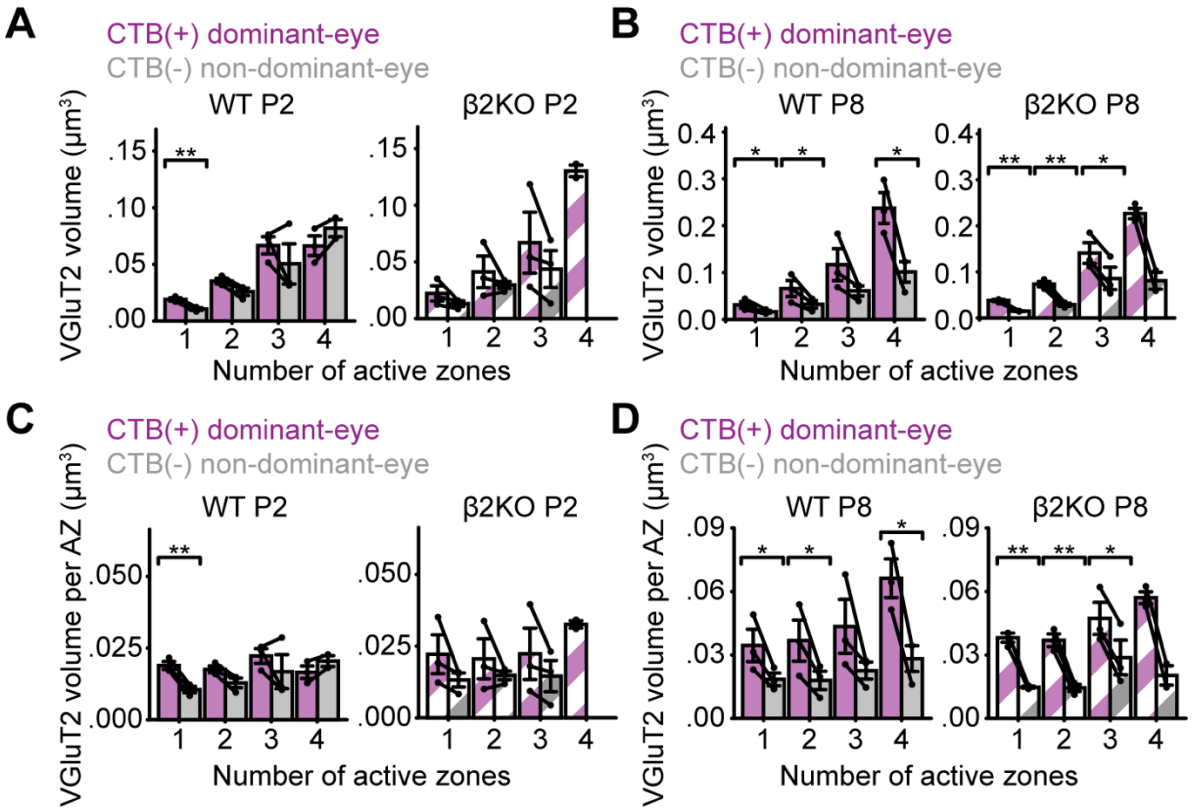

Figure S2: mAZ synapses undergo eye-specific vesicle pool maturation, related to Figure 2. (A-B) VGluT2 cluster volume relative to AZ number for each synapse in WT (left panels) and β2KO mice (right panels) at P2 (A) and P8 (B). (C-D) Average VGluT2 volume per AZ (bassoon cluster) for all synapses in WT (left panels) and β2KO mice (right panels) at P2 (C) and P8 (D). For all panels, error bars indicate means ± SEMs (N=3 biological replicates for each age and genotype). Black dots represent mean values from separate biological replicates and black lines connect measurements within each replicate. Statistical significance between eye-specific synapse measurements was assessed using paired T-tests: *: p<0.05; **:p<0.01.

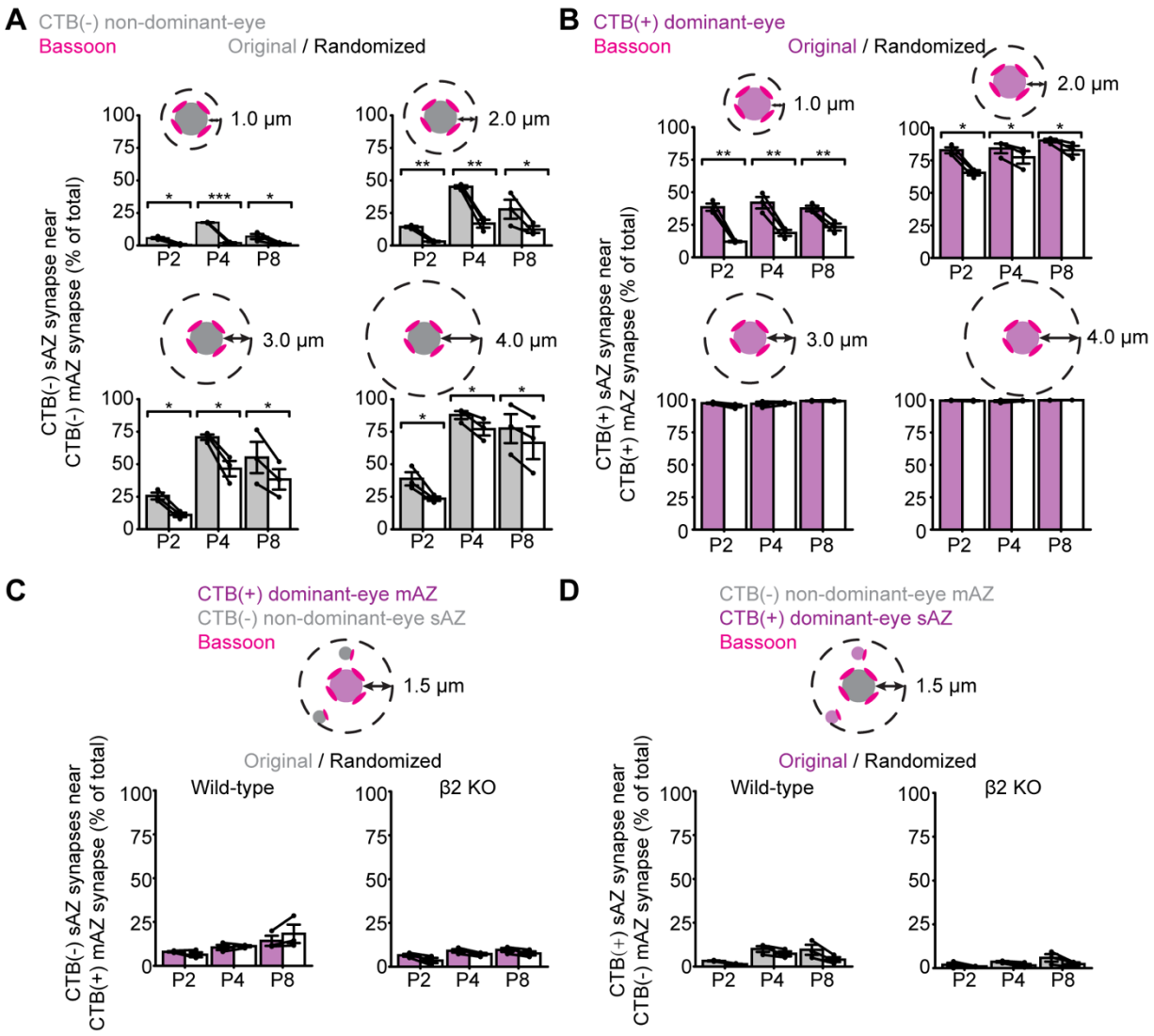

Figure S3: Eye-specific and distance-dependent synapse clustering, related to Figure 3. (A) The ratio of CTB(-) sAZ synapses nearby like-eye mAZ synapses for increasing distance thresholds in WT P4 samples. The observed ratios are higher than a reshuffling of the data at distances of 1-4 µm across all time points. (B) Same presentation of results as in (A), but for CTB(+) sAZ synapses nearby CTB(+) mAZ synapses. (C) Percentage of CTB(-) non-dominant-eye sAZ synapses within 1.5 µm of an opposite-eye CTB(+) mAZ synapse in WT (left panel) and β2KO mice (right panel) at P4. (D) Same presentation as in (C), showing percentage of CTB(+) dominant-eye sAZ

synapses near an opposite-eye mAZ synapse. For all panels, error bars represent means ± SEMs (N=3 biological replicates for each age and genotype). Black dots represent mean values from separate biological replicates and black lines connect measurements within each replicate. Statistical significance between original and shuffled measurements was assessed using paired T-tests: *: P<0.05; **: p<0.01; ***: p<0.001.

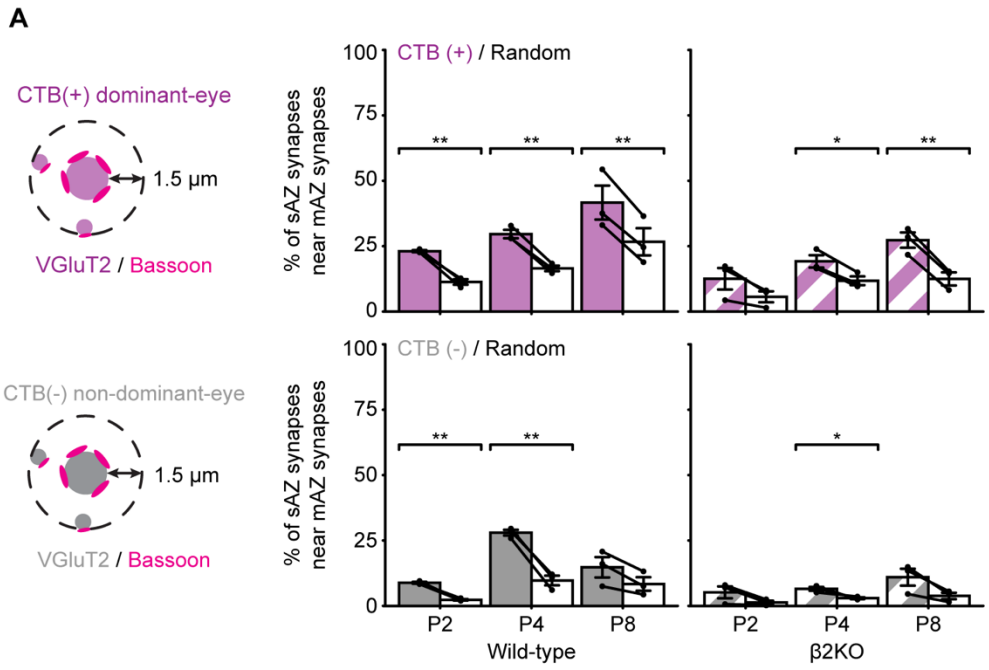

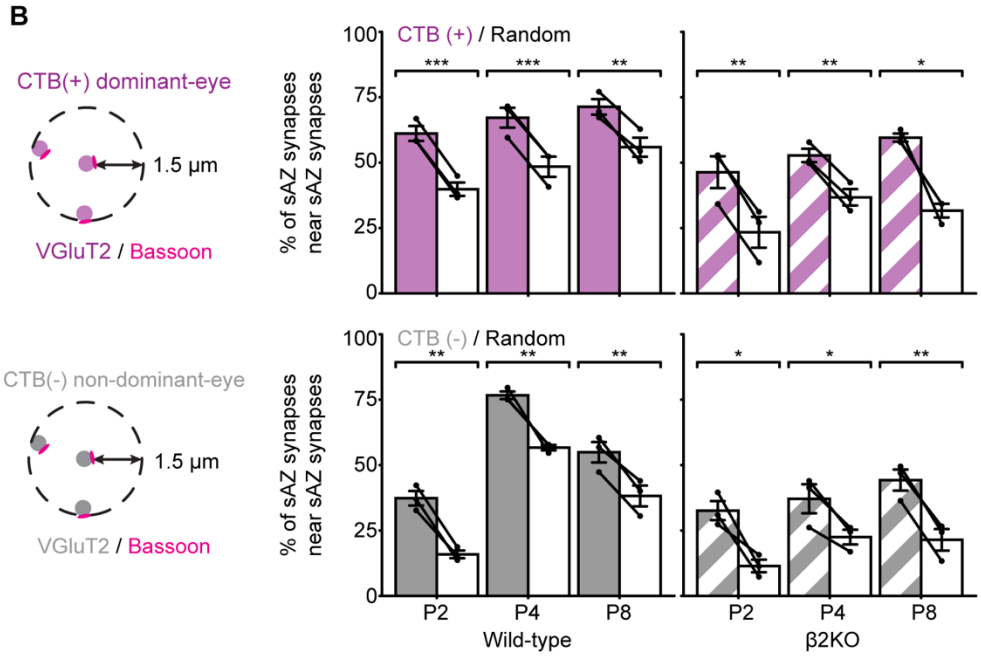

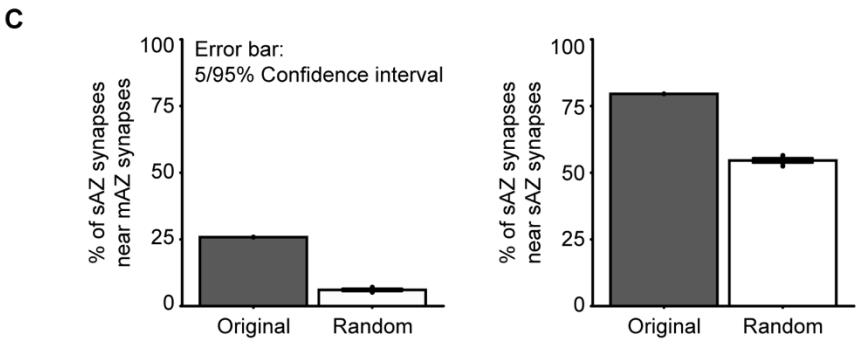

1079

Figure S4: Multi-active zone synapses are loci for synaptic clustering. (A) Comparison of the total percentage of dominant-eye (top panels) and non-dominant (bottom panels) sAZ synapses near like-eye mAZ synapses between the original and shuffled synapse positions across all time points. Left panels: WT; Right panels: β2KO. (B) Same analysis as in (A) but comparing the total percentage of sAZ synapses near like-eye sAZ synapses. Error bars represent means ± SEMs (N=3 biological replicates). Black dots represent mean values from separate biological replicates and black lines connect measurements between measured and shuffled values for each replicate. Statistical significance between original and shuffled measurements was assessed using paired T-tests: *: P<0.05; **: p<0.01; ***: p<0.001. (C) Comparison between the original data and 10 iterations of data shuffling from a WTP4 CTB(-) sample (left) and a WTP4 CTB(+) sample (right). Error bars represent 5/95% confidence intervals.

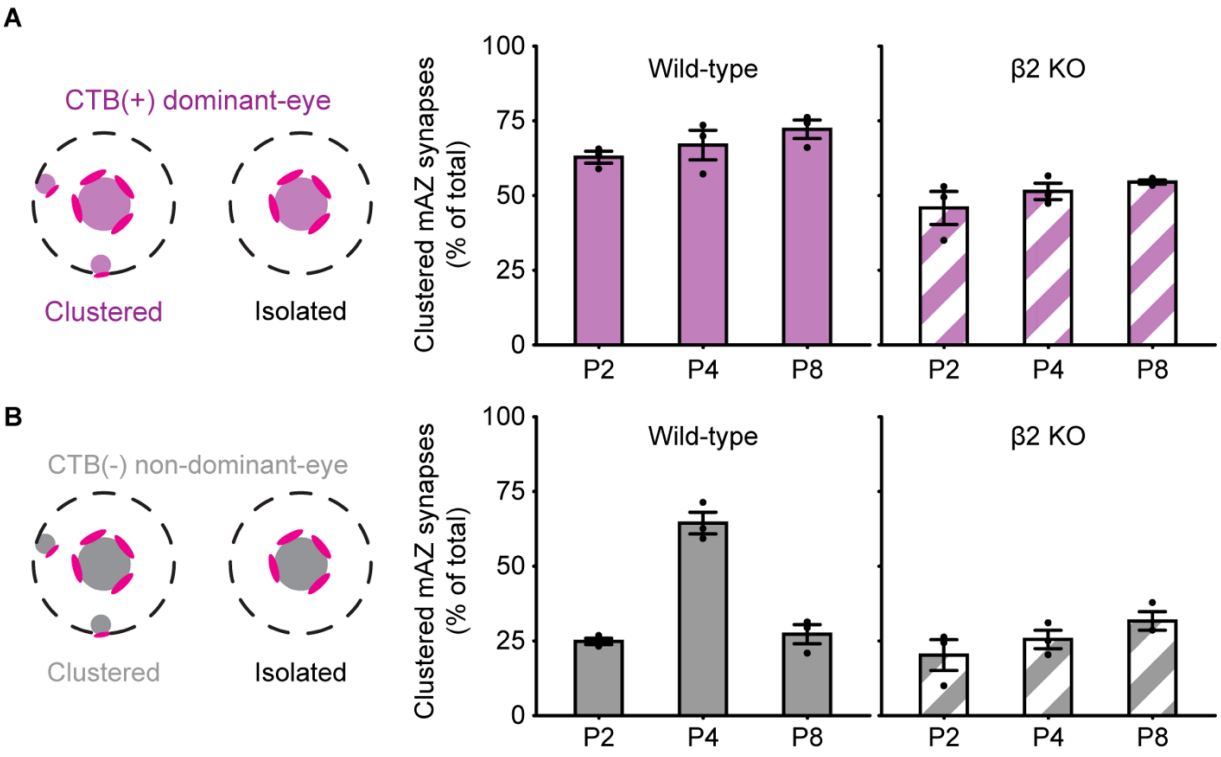

Figure S5 : The ratio of clustered and isolated eye-specific mAZ synapses, related to Figure 4. Clustered and isolated mAZ synapses are distinguished by the presence of sAZ synapses within a 1.5 μm radius shell. The figures show the ratio of clustered mAZ synapses for CTB(+) (A) and CTB(-) (B) synapses.

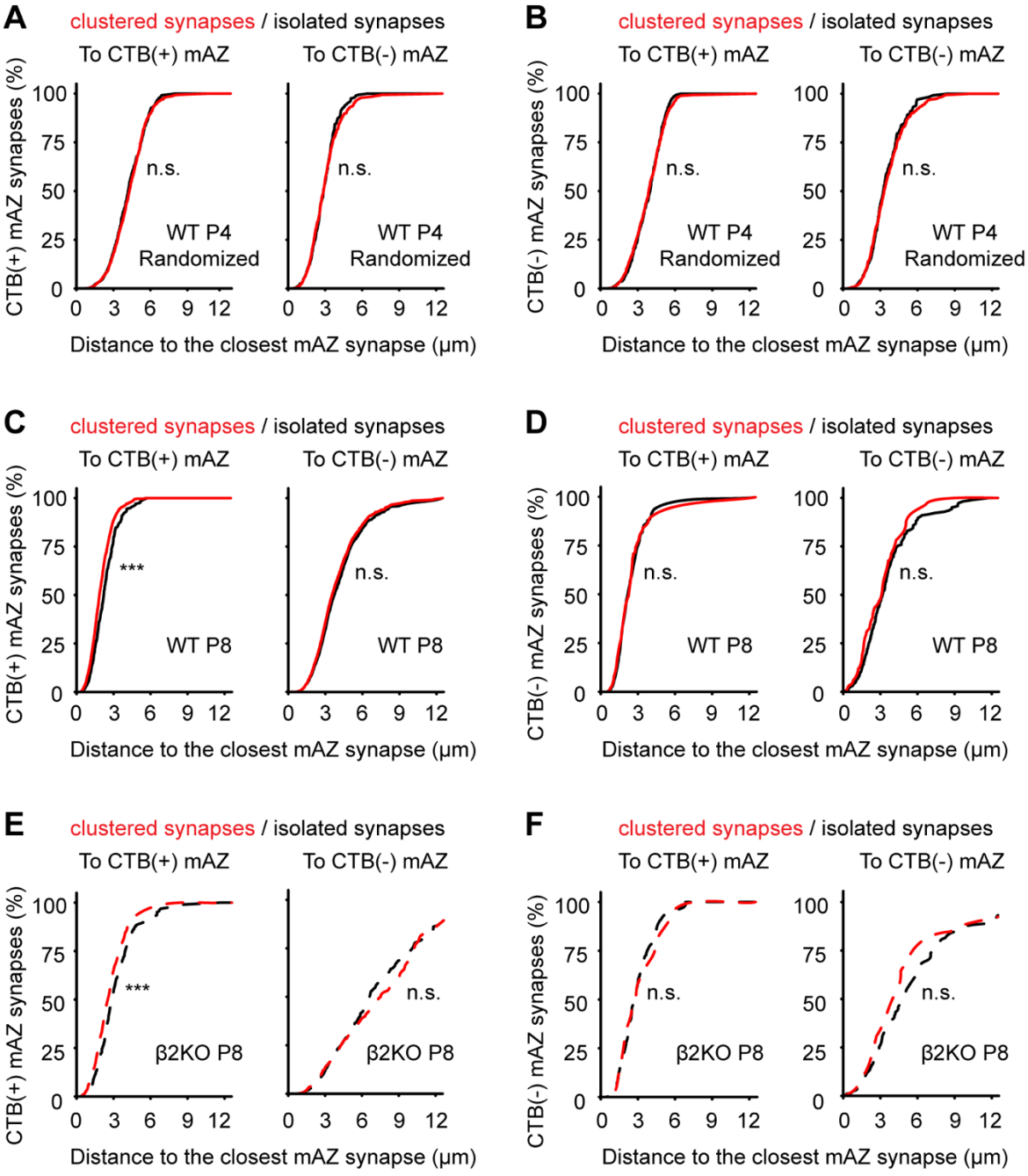

Figure S6: Eye-specific synaptic clustering varies based on distance to multi-active zone synapses, related to Figure 4. (A) Cumulative histogram of the distances from CTB(+) mAZ synapses to their nearest CTB(+) (left panel) and CTB(-) (right panel) mAZ synapse in P4 WT data where sAZ synapse distributions were randomized. Black lines show distributions for isolated mAZ synapses with no nearby (<1.5 μm) sAZ

synapses and red lines show distributions for clustered mAZ synapses with one or more sAZ synapses nearby. (B) Same presentation as in (A), showing distances from CTB(-) mAZ synapses to their nearest CTB(+) (left panel) and CTB(-) (right panel) mAZ synapse in P4 WT randomized data. (C and D) Same presentation as in A/B, showing WT P8 original data. (E and F) Same presentation as in C/D, showing β2KO P8 original data. Nonparametric Kolmogorov-Smirnov tests were used for statistical comparisons (N=3 biological replicates for each condition). ***: $p<0.001$. "n.s." indicates no significant differences. Separate measurements of 5/95% confidence intervals show overlap of the two distributions in each “n.s.” instance.

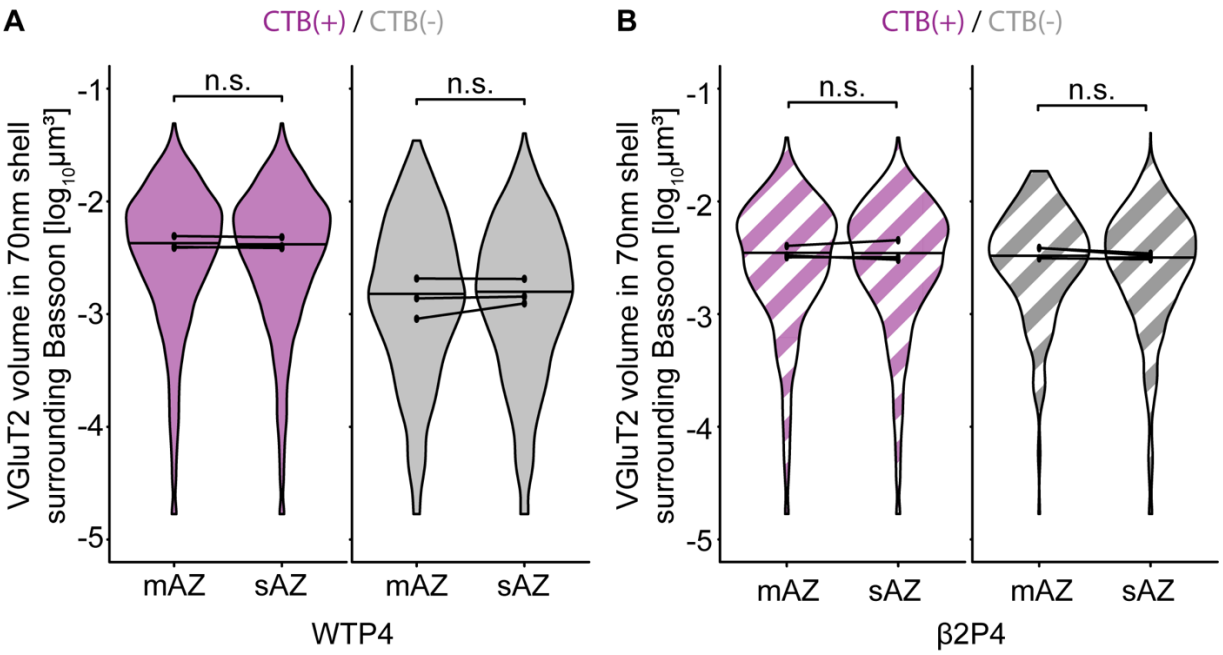

Figure S7: VGluT2 volume near active zones is similar between multi-AZ and single-AZ synapses at P4.

(A) The violin plots show the distribution of VGluT2 volume within a 70nm shell surrounding each associated Bassoon cluster (AZ). The width of each violin plot reflects the relative synapse proportions at each volume across the entire grouped data set (N=3 biological replicates). The maximum width of the violin plots was normalized across mAZ and sAZ groups. The black dots represent the median value of each biological replicate (N=3), and the black horizontal lines represent the median value of all synapses grouped across replicates. Black lines connect measurements of sAZ and mAZ populations from the same biological replicate. Statistical significance was determined using a mixed model ANOVA. “n.s.” represents that no significant differences were found. Measurements of 5/95% confidence intervals show overlap of the two distributions in each “n.s.” instance. (B) VGluT2 signal volume near the AZ is

similar for mAZ and sAZ synapses in β2KO mice. Data presentation and statistics are the same as those in (A).